MSc Interaction Technology
Master Thesis

# Human and Pet Vital Sign Detection and Activity Recognition by Using a mmWave FMCW Radar

Karina Skurule

April 2, 2024

**Supervisor**:
Ehsan Sam Sadeghi

**Graduation committee:**
dr. ing. Gwenn Englebienne, prof. dr. Paul Havinga

Department of Pervasive Systems
Faculty of Electrical Engineering,
Mathematics and Computer Science,
University of Twente

**UNIVERSITY OF TWENTE.**

# Abstract

This master's thesis investigates the applicationof Frequency-Modulated Continuous-Wave (FMCW) radar technology for non-invasive monitoring of vital signs and activity recognition in humans and pets. Addressing the limitations of traditional contact-based sensors and wearables, which include discomfort, stress, movement artifacts, and privacy concerns, this research demonstrates the radar technology's capability as a versatile, accurate, and non-intrusive alternative.

The operational principles of FMCW radar are explored, emphasizing its adeptness at detecting minute physiological movements that indicate heart and breathing rates. Experiments with human subjects, including those with unique conditions like meditation expertise and asthma, provide a comparative analysis of various signal processing algorithms—such as DC offset correction by Nonlinear Least Squares (NLLS) and Gradient Descent algorithm, phase calculation by Differentiate and Cross-Multiply (DACM) and Extended DACM (EDACM), and vital sign estimation by Fast Fourier Transform (FFT), the Rife Algorithm, and Peak Counting. The results high light the technology's precision, with an error rate as low as 3.98 breaths per minute (bpm) for heart rate and 6.92 bpm for breathing rate in human subjects.

For pets, the study shows the radar's efficacy in breathing rate estimation, with improved accuracy at closer distances and an error rate as low as 2.26 bpm. Activity recognition extends the radar's application, with a Support Vector Machine (SVM) classifier achieving 74.77% accuracy in classifying six distinct activities for cats and humans, illustrating the depth of radar technology in monitoring health and behavior.

This research confirms mmWave FMCW radar technology's potential to transform non-invasive health monitoring. Offering a stress-free, contactless, and precise method for vital sign detection and activity recognition, it sets a foundation for advancements that could better healthcare and veterinary care, improving well-being through innovative monitoring solutions.

**Keywords:** mmWave FMCW radar technology, non-invasive monitoring, vital signs, activity recognition, signal processing algorithms, healthcare, veterinary care.

# Contents

# List of Tables

# List of Figures

# Chapter 1

# Introduction

## 1.1 Problem Statement

The evolution of health monitoring technologies has significantly influenced both human and animal healthcare, fostering advancements in the diagnosis, treatment, and continuous care of various conditions. Despite these advancements, current monitoring methods, particularly those involving direct contact or wearables, face challenges such as discomfort, the potential for inaccuracies due to movement artefacts, and, in the case of animals, stress and behavioral interference [47, 14, 4, 27]. These limitations underscore the necessity for innovative approaches that prioritize non-invasiveness and accuracy.

Radar technology, such as mmWave FMCW radar, emerges as a promising solution to these challenges. Radar can be used to detect minute physiological movements caused by heartbeats and respiration, hence, offering a seamless, non-contact method for monitoring vital signs such as Heart Rate (HR) and Breathing Rate (BR) [55, 72]. The potential of radar-based monitoring extends beyond human healthcare, providing a non-invasive method for monitoring animal health. This approach is particularly advantageous for monitoring vital signs in animals, where traditional methods may cause stress or discomfort, leading to inaccurate readings [103, 36].

Moreover, the integration of radar technology in monitoring systems supports the continuous, real-time observation of health indicators in diverse environments. For humans, it can enhance patient care in homes, hospitals, and care facilities by facilitating early detection of conditions like cardiovascular diseases and respiratory issues [95, 52]. For animals, it aids in the identification and management of health issues such as pain, anxiety, fever, and heart or breathing diseases, which are critical for both domestic pets and livestock [67, 38, 91].

Furthermore, the application of radar technology in activity recognition opens new possibilities for comprehensive health and behavioral monitoring. Recognizing activities such as eating, walking, or jumping in pets, for instance, contributes valuable insights into their well-being, enhancing the ability to detect and respond to health issues promptly. This is particularly relevant in scenarios involving the cohabitation of elderly people and their pets, where simultaneous monitoring could provide critical data for ensuring the health and safety of both.

The dual focus on vital sign detection and activity recognition through mmWave FMCW radar technology reflects a comprehensive approach to health monitoring. By addressing the specific needs and challenges associated with human and animal health monitoring, this technology stands out as a versatile, non-invasive solution that respects privacy concerns and overcomes the limitations of wearables and direct contact sensors.

## 1.2 Research Questions

This research is guided by a primary question focused on the exploration of mmWave FMCW radar technology's role in non-invasive health monitoring for humans and pets. Subsequent sub-questions delve into the specifics of technology application, signal processing, comparative accuracy, activity recognition, and empirical validation.

### 1.2.1 Main Research Question

- **What is the potential of mmWave FMCW radar technology in enhancing non-invasive health monitoring for humans and pets?**

### 1.2.2 Sub-Questions

1. How does FMCW radar technology operate, and why is it suitable for non-invasive monitoring of vital signs such as HR and BR in humans and animals?

2. What signal processing algorithms are necessary for accurately extracting vital sign information (HR and BR) from radar signals?

3. How do these algorithms differ between human and animal monitoring?

4. How can FMCW radar technology be applied to recognize and classify different animal activities, and what are the implications of these capabilities for understanding animal behavior and health?

By addressing these research questions, the study aims to investigate the viability, efficacy, and broader implications of employing mmWave FMCW radar technology for non-invasive health monitoring purposes, thereby contributing to the advancement of healthcare and veterinary care practices.

## 1.3 Outline

The thesis is organized to offer a comprehensive exploration into the utilization of mmWave FMCW radar technology for non-invasive health monitoring. Chapter 2 presents the State of the Art, providing a critical review of current technologies and methodologies for detecting vital signs and recognizing activities, with a focus on both human and animal applications. Chapter 3 delves into the Vital Signs Physiological Fundamentals, discussing the biological underpinnings of vital signs and comparing contact versus non-contact measurement devices. Chapter 4, Radars, introduces radar technology fundamentals, emphasizing mmWave and FMCW radars, and their relevance to vital sign detection. In Chapter 5, Hardware Overview, the selection and optimization of radar configurations for vital sign detection and activity recognition are discussed.

Vital Sign Signal Processing techniques employed in this study are outlined in Chapter 6. The experimental results from monitoring human vital signs are presented in Chapter 7, including methodological challenges and achieved accuracies. Chapter 8 reports on the application of radar technology in monitoring pets' vital signs, reflecting on the experimental approach and findings.

Chapter 9 extends the discussion to Activity Recognition Signal Processing, detailing the process of capturing and analyzing micro-Doppler signatures for activity differentiation. Chapter 10 focuses on Activity Recognition, exploring the efficacy of machine learning

classifiers in identifying different activities based on radar data, and comparing model performances.

Finally, Chapter 11 concludes the thesis by summarizing the key insights, answering the research questions, and suggesting directions for future research. Appendices provide supplementary materials such as the dataset article, examples of micro-Doppler spectrograms, and classifier test confusion matrices.

# Chapter 2

# State of the Art

## 2.1 Vital Signs

The evolution from wearable to non-wearable sensor technologies has contributed to advancements in vital sign monitoring, a critical component for diagnosing and managing health conditions. This chapter provides a focused review on the development and application of these technologies, with an emphasis on radar systems for non-invasive detection of HR and BR.

### 2.1.1 Human Wearable and Non-wearable Sensors for Vital Sign Detection

Wearable devices, such as smartwatches and chest straps, have become relevant due to their convenience and real-time monitoring capabilities [6, 3, 5]. Despite their widespread use, the search for more seamless methods has led to the exploration of non-wearable technologies, including radar and camera-based systems, offering the potential for more comfortable and less invasive monitoring [10, 65].

Radar technology, in particular, has emerged as a promising non-wearable approach. Its advantage lies in its ability to penetrate clothing and operate unaffected by ambient environmental conditions, a significant limitation of optical-based sensors. Also, radar technology does not threaten ones privacy. Among various radar types—Ultra Wide Band (UWB), Stepped Frequency Continuous Wave (SFCW), Continuous Wave (CW), and Frequency Modulated Continuous Wave (FMCW)—each has shown potential in vital sign detection with varying degrees of accuracy and operational benefits [54, 32].

- UWB radars, operating at 24GHz, have demonstrated an HR error rate of just 1%, indicating high precision in detecting heartbeats [84].

- SFCW radars in the 2-4GHz range achieved a 1.6% HR error, showcasing their reliability in heart rate monitoring [79].

- CW radars at 14GHz reported a 2.2% HR error rate, further validating radar technology's effectiveness in vital sign detection [53].

- FMCW radars, particularly in the 75-85GHz spectrum, while achieving an HR error rate of 8.09% and a BR error rate of 6.89%, highlight the technology's potential for detailed and accurate measurements of both heart and breathing rates due to their high resolution [110].

The measurement setups across these studies varied, with differences in distance from the radar and specific signal processing techniques applied, indicating the importance of context in evaluating radar performance. Additionally, the integration of radar with camera systems has been explored to mitigate motion-induced signal distortion, enhancing measurement accuracy by compensating for random body movements [32].

FMCW radar's ability to operate at high frequencies for improved resolution and its capacity to determine the speed, distance, and angle of objects make it a focal point of this research [22]. The subsequent sections will delve into the specific signal processing techniques and experimental setups employed in this work, showing the possibly promising application of FMCW radar in vital sign monitoring.

### 2.1.2 Human Vital Sign Detection by FMCW Radar

FMCW radar stands out in resent research for its precision in human HR and BR monitoring. Various studies have employed FMCW radar alongside distinct signal processing methods to optimize accuracy. The general processing sequence involves identifying the target via range bin detection, phase signal calculation for chest displacement, filtering to isolate HR and BR frequencies, and final HR and BR rate determination. The final stage - HR and BR rate estimation - can be divided into the two following groups.

**Decomposition-Based Methods**

Decomposition techniques like Variational Mode Decomposition (VMD) and its adaptations (e.g., AVMD, Iterative VMD) alongside Ensemble Empirical Mode Decomposition (EEMD) are employed for their proficiency in segregating signals into intrinsic mode functions (IMFs). These IMFs facilitate the extraction of heart and breathing rates by isolating specific signal components.

**Adaptive Variational Mode Decomposition (AVMD):** Walid et al. (2022) used AVMD to enhance FMCW radar's vital sign monitoring accuracy, demonstrating the advantage of AVMD over traditional VMD and filtering methods. Their adaptive approach, starting with a initial estimation using peak counting or strongest frequency component selection, resulted in notable accuracy improvements, particularly in HR detection, with an MAE of 0.62 for BR and 3.95 for HR at a 1.4m distance and zero angle [104].

**Iterative VMD Wavelet-Interval-Thresholding:** Xiang et al. (2022) introduced a comprehensive signal processing framework, beginning with Range-FFT and extending to advanced noise reduction via Iterative VMD Wavelet-Interval-Thresholding. Their hybrid HR extraction algorithm combined FFT with chirp Z-transform (CZT) techniques, achieving relative errors of 1.33% for BR and 1.96% for HR, demonstrating the efficacy of their methodology [112].

**CEEMDAN and MUSIC Algorithm:** Sun et al. (2020) employed CEEMDAN for noise reduction and the Multiple Signal Classification (MUSIC) algorithm for HR signal separation. Their method showcased promising HR estimation accuracy with an RMSE less than 6 bpm, highlighting the potential of CEEMDAN and MUSIC in vital sign monitoring [98].

**ICEEMDAN and Fast-ICA:** Yang et al. (2023) utilized Improved Complete Ensemble Empirical Mode Decomposition with Adaptive Noise (ICEEMDAN) and Fast Independent Component Analysis (Fast-ICA) for heartbeat signal stabilization and noise reduction. Their approach focused exclusively on HR estimation, reporting a mean absolute error (MAE) of less than 4 bpm over short durations, underscoring the precision of their signal processing scheme [115].

**Comprehensive Signal Processing Scheme:** Zhao et al. (2022) developed a novel signal processing strategy incorporating Range-FFT, target detection, and advanced denoising techniques to reconstruct the heartbeat signal accurately. Their method demonstrated an RMSE of less than 3 bpm, with MAPE also below 3%, validating the effectiveness of their approach in HR estimation without focusing on BR [118].

Each study presents a unique methodological framework, from signal decomposition to the advanced filtering and denoising techniques, illustrating the diverse signal processing approaches possible within FMCW radar technology for vital sign monitoring. These methods lay the groundwork for further refining and optimizing FMCW radar-based systems for accurate, non-invasive human vital sign detection.

### Filter-Based Methods

Filter-based approaches, employing techniques such as Fast Fourier Transform (FFT) alongside peak detection, bandpass filters, Finite Impulse Response (FIR) filters, and the Rife algorithm, are pivotal for isolating frequencies related to vital physiological activities. These methods are valued for their straightforward application and efficacy in highlighting specific frequency ranges indicative of heart and breathing rates.

**Phase Demodulation and Band-pass Filtering:** Srihari et al. (2021) utilize phase demodulation, smoothing, normalization, and band-pass filtering to differentiate HR and BR. The methodology emphasizes band-pass filters for frequency isolation, achieving a mean error percentage (MEP) of 4.79% for HR from 20 volunteers, without explicitly detailing BR comparison [97].

**Differential Operation and Kalman Filter:** Ji et al. (2021) integrate Range-FFT, phase extraction, differential operation for HR detection, and Kalman filtering for signal enhancement. The method uses FIR band-pass filtering to eliminate breathing signals, reporting HR estimation errors ranging from 1.97% to 4.26% across five subjects [45].

**Kalman Filtering and Rife Algorithm:** Chen et al. (2022) propose a method that combines Range-FFT, phase unwrapping, and Kalman filtering, supplemented by the Rife algorithm for HR estimation. This approach yields an RMSE of less than 3.4 bpm for HR in 10 subjects, demonstrating the precision of the filtering and estimation techniques used [19].

**Survey of Contactless Monitoring Algorithms:** Giordano et al. (2022) evaluate various algorithms for contactless vital sign monitoring, utilizing band-pass filtering and FFT/STFT for HR and BR measurement. Their study, which encompasses multiple radar technologies, highlights a median-FFT combination as particularly effective, with an average relative error of 7.4% for HR using different radar systems [30].

**Enhanced Detection Techniques:** Alizadeh et al. (2019) present a method achieving up to 80% accuracy for HR and 94% for BR, incorporating a unique DC compensation technique and advanced phase unwrapping manipulation. Liu et al. (2020) introduce a coarse-to-fine estimation technique for HR, predicting the heartbeat rate from the unwrapped phase signal and employing an adaptive threshold for filtering, alongside spectral estimation for BR detection [9, 57].

These studies collectively underscore the versatility and effectiveness of filter-based methods in vital sign monitoring using FMCW radar. By strategically applying various filtering and peak detection techniques, researchers have successfully isolated heart and breathing rates from radar signals, marking significant advancements in non-invasive health monitoring technology.

**MIMO-Based Techniques**

MIMO (Multiple-Input Multiple-Output) technology, leveraging multiple antennas at both the transmitter and receiver, marks a significant evolution from the Single-Input Single-Output (SISO) configuration, which was used in the previously mentioned studies. By exploiting the spatial domain, MIMO enhances spectral efficiency, increases data throughput, and improves the resolution and object differentiation capabilities of FMCW mmWave radar systems [34]. This section explores the application of MIMO configurations in FMCW radar for vital sign detection, highlighting various signal processing techniques that benefit from MIMO's advanced capabilities.

The integration of MIMO in FMCW radar systems substantially impacts the Signal to Noise Ratio (SNR) and, consequently, the accuracy of HR and BR detection. Oleksak et al. (2020) investigate different signal processing methods applied to 60GHz and 77GHz FMCW systems, including State Space Method (SSM), Time Varying Window (TVW), and Feature-Based Correlation and Topological Similarity (FBTS), among others. The study emphasizes the effectiveness of SSM-Arctangent Demodulation Bandpass (SSM-AD BP), achieving the lowest HR percentage error of 1.2% at 60GHz and 1% at 77GHz from a 1-meter distance with MIMO channel processing. Notably, the 60GHz system demonstrates superior performance, attributed to the 77GHz system's heightened sensitivity to body movements. Nevertheless, higher frequency radars offer improved resolution, enhancing HR and BR detection accuracy [70].

Wang et al. (2020) detail a compressive sensing approach based on the orthogonal matching pursuit (CS-OMP) algorithm and adaptive soft threshold noise reduction via discrete wavelet transform (RA-DWT). Their method, which includes FFT and time-domain auto-correlation for HR detection, showcases a 93% accuracy, benefiting from the high-resolution capabilities of MIMO radar systems. The study also incorporates circular center dynamic tracking for DC offset correction and extended DACM for phase unwrapping, further illustrating the advanced signal processing potential of MIMO configurations [111].

Additionally, MIMO radar systems are adept at positioning detection alongside vital sign monitoring. Huang et al. (2019) demonstrate simultaneous location and parameter estimation using multiple channel echoes. Their approach employs range pulse compressing and azimuth Capon beamforming to generate range azimuth heat-maps for estimating the range and azimuth of human targets. This method highlights MIMO's dual utility in precise positioning and vital sign detection, though it does not explicitly report the error rate for HR detection [40].

MIMO technology, with its advanced spatial exploitation and enhanced resolution, presents a robust framework for improving vital sign detection accuracy and reliability in FMCW radar systems. The application of sophisticated signal processing techniques within MIMO configurations underscores the technology's potential to redefine non-invasive health monitoring.

**AI Integration for Enhanced Vital Sign Detection**

The incorporation of Artificial Intelligence (AI) into radar-based vital sign detection presents a novel frontier for improving the accuracy of HR and BR measurements. Despite its emergent status, AI's potential to refine vital sign detection, especially amidst challenges like random body movements, is increasingly recognized.

**Convolutional Neural Networks for Body Part Recognition:** The utilization of AI, particularly Convolutional Neural Networks (CNNs), for identifying human body parts and postures, marks a significant advancement. This AI application enables precise

chest location estimation, critical for accurate vital sign extraction. Alidoustaghdam, Hadi, et al. (2023) demonstrate an approach where AI-enhanced recognition facilitates targeted beamforming in a MIMO setup, significantly boosting the SNR. Despite the lack of explicit accuracy figures, this method underscores AI's capacity to isolate vital signs by focusing on the chest area, employing phase DC compensation and subsequent signal processing techniques [8].

**Camera-assisted Chest Location Estimation:** Shokouhmand, Arash, et al. (2022) explore a synergistic method combining camera technology and FMCW radar for chest location estimation, thereby enhancing HR and BR detection accuracy. Their findings reveal impressive detection accuracies—ranging from 90.02% to 97.68% for BR and 89.50% to 95.88% for HR—across distances of 0.5m to 2.5m, showcasing the efficacy of integrating visual cues with radar measurements for vital sign monitoring [92].

**Deep Neural Networks for Motion Cancellation:** Gu, Changzhan, et al. (2019) introduce the use of deep neural networks (DNN) to counteract the interference of random body movements on vital sign detection. By synthesizing breathing motions with varying frequencies and phases, their DNN model learns to predict BR motion with remarkable stability, illustrating AI's potential to enhance signal clarity and measurement reliability [33].

The emerging applications of AI in radar-based vital sign monitoring highlight a promising convergence of technologies. AI's capability to address the complexities of human movement and physiology significantly contributes to the development of more accurate, non-invasive health monitoring systems. However, the exploration of AI in this domain is still in its infancy, with substantial potential for further research and innovation.

### 2.1.3 Animal Non-wearable Sensors for Vital Sign Detection

Non-invasive monitoring of animal vital signs presents unique challenges, necessitating methods that minimize stress and discomfort. While traditional approaches often involve direct contact, emerging non-wearable technologies offer promising alternatives for stress-free monitoring [82].

Innovative methods include:

- **Infrared (IR) Sensors:** Employed for intertidal animals like mussels, allowing vital sign detection through the animal's shell, providing a non-contact means of HR monitoring [15].

- **Thermal Imaging:** Utilizes thermal cameras to detect skin temperature fluctuations corresponding to heartbeats, translating these into HR measurements [48].

- **Photoplethysmography:** Measures pulse through skin color changes, offering another non-contact method for HR and BR detection [102].

Radar technology, particularly Doppler and FMCW, has been applied to remotely monitor animal vital signs with varying degrees of success:

- **CW Doppler Radar:** Demonstrated potential in detecting cat vital signs beneath the animal, though accuracy specifics are not mentioned due to the lack of reference sensors [51]. In paper [21], a custom 100 GHz CW Doppler radar was used to detect the BR and HR of a rat and a rabbit. The measurements were made in a laboratory setting, where animals were sleeping under anesthesia. No reference sensor was used. In study [41], a 60 GHz CW Doppler radar was used, and the results show an average error rate of 0.057% for BR and 0.33% for HR from three rat test subjects. The

distance was 0.3 meters between the test rat and the radar, and the tested rats were in a chamber under anesthesia. In [75], a 24 GHz CW Doppler radar is used to measure BR and HR in chickens, which shows an accuracy of up to 96%. The radar was placed close to the chest of the tightly held test subjects - 0.18 meters. As a reference, contact based reference ECG module was used.

- **UWB Radar:** Showed efficacy in distinguishing vital signs of dogs, cats, and rabbits, highlighting the capability to differentiate between species without direct contact [109]. In [108], UWB radar was used on dogs and cats, and in [64], UWB Bio radar was used on dogs. In these two studies ECG was used as a reference sensor, and the animals were under anesthesia.

- **FMCW Radar:** In study [114], the authors indicated high accuracy in BR and HR detection in pets, with VMD algorithm performance surpassing other tested methods. This study shows BR accuracy of 98.7% and HR accuracy of 97.7% with the test subject being a dog in a cage. The study fails to mention what is the reference sensor.

Despite promising developments, the exploration of radar-based, non-wearable technologies for animal vital sign monitoring in the process of development, with significant potential for advancement in achieving high-accuracy, stress-free monitoring.

## 2.2 Activity Recognition

Activity Recognition (AR) significantly benefits healthcare, security, animal welfare, and more. For humans, AR facilitates quality of life improvements, particularly for the elderly or chronically ill, through continuous monitoring and anomaly detection. In security, recognizing human activities aids in identifying potential threats. Similarly, in animal care and conservation, AR offers insights into health, well-being, and behavior, critical for early illness detection and species preservation efforts.

Radar technology, particularly via micro-Doppler spectrograms, plays a vital role in AR by offering non-invasive, accurate activity capture. This section explores methodological advancements in Human Activity Recognition (HAR) and Animal Activity Recognition (AAR), underscoring radar's utility in diverse AR applications.

### 2.2.1 Human Activity Recognition

**Diverse Activity Detection:** Broeder et al. analyze activities like clapping and jogging through micro-Doppler spectrograms, using classifiers such as SVM, LSTM, and CNN+LSTM, achieving accuracies up to 99.83%. The study's success, attributed to distinct activity selection and advanced filtering techniques, illustrates radar's capability in HAR [13].

**Daily Activity Classification:** Li, Haobo, et al. employ bi-LSTM for classifying activities like walking and sitting, reaching approximately 96% accuracy. Their approach, featuring FFT and STFT for signal processing, showcases the effectiveness of deep learning in enhancing HAR [56].

**Multi-Activity Recognition:** Kim et al.'s study includes a broad range of activities, utilizing SVM for over 90% classification accuracy. This work highlights SVM's utility in HAR, benefiting from a decision-tree structure for efficient training and testing [50].

**CNN for Motion Behavior Detection:** Zhang et al. utilize CNN for detecting motions, achieving accuracies between 64% and 99.59%. Their method emphasizes CNN's role in processing unvisualized micro-Doppler signatures for HAR [117].

**Gait Recognition:** Janakaraj et al. focus on gait recognition using a custom DNN, demonstrating a 97.45% accuracy rate. Their process for target tracking and identification via radar data processing methods, like CA-CFAR, underlines the precision of DNNs in HAR [44].

**Dynamic Hand Gesture Recognition:** Jiang et al. achieve up to 95.2% accuracy in recognizing dynamic hand gestures with CNN, outperforming SVM in various scenarios. This study exemplifies CNN's superiority in detailed activity classification [46].

**Environment-specific HAR:** Shah et al. compare SVM, KNN, and GoogleNet across different environments, with GoogleNet providing 68.5% to 81% accuracy. Their work highlights the challenges and potential of implementing HAR in varying conditions [90].

### 2.2.2 Animal Activity Recognition

**Dog Activity Recognition:** In study by Raalte et al., point cloud data from radar is employed for dog activities, testing activities like sitting and walking. Classifiers such as SVM and LSTM were used, reaching up to 72.45% accuracy, showcasing the early potential of radar in AAR [74].

**Monitoring Lameness in Domestic Animals:** Shrestha's work on detecting lameness in animals like cows and sheep through FMCW radar and classifiers like SVM-Q and KNN shows high accuracy levels. This research highlights radar's potential in identifying health issues in animals [93]. The true lame versus predicted lame percentage was 91.40% for dairy cows, 87.7% for horses. The sheep confusion matrix seems to not be provided, but the recorded accuracy is reported to be 100% for sheep.

Best of the author knowledge, there are no other studies exploring the AAR. There are, however, studies only working with animal recognition and human recognition from animals and other objects [60, 37]. These studies collectively demonstrate the growing scope of radar technology in activity recognition, highlighting the integration of machine learning for enhanced accuracy in both HAR and AAR. The ongoing research and development in this field promise significant advancements in non-invasive monitoring for both human and animal welfare.

# Chapter 3

# Vital Signs Physiological Fundamentals

Understanding the physiological underpinnings of the cardiovascular and respiratory systems is essential for accurately interpreting vital sign signals obtained via mmWave radar FMCW. This chapter describes the basics of cardiovascular and breathing physiology, emphasizing elements pertinent to HR and BR analysis for both humans and cats.

## 3.1 Cardiovascular Physiology

The cardiovascular system is integral for circulating oxygen, nutrients, and other vital substances throughout the body. In the context of HR analysis, several concepts are important:

- HR and HR Variability (HRV): Reflects the variations in time intervals between successive heartbeats, signaling the heart's responsiveness to physiological and environmental stimuli. It is a crucial indicator of stress and emotional states in both humans and animals [88, 25].

- Human HR: A normal resting HR for adults spans from 60 to 100 bpm, influenced by factors like fitness level and emotional state [26].

- Cat HR: A resting cat's HR varies around 132 ($\pm$19) bpm at home and can elevate to approximately 187 ($\pm$25) bpm when restrained, demonstrating the impact of environmental conditions on physiological responses [7].

## 3.2 Breathing Physiology

Breathing involves inhaling oxygen and exhaling carbon dioxide, facilitated by the coordinated action of the lungs and respiratory muscles. For BR analysis, understanding the following aspects is essential:

- Chest Displacement: The lung volume changes during respiration cause measurable chest displacement, serving as a basis for BR estimation through various non-invasive techniques [76].

- BR Variability (BRV): Analogous to HRV, BRV assesses the variation in breathing intervals, providing insights into respiratory control and the impact of physiological and psychological factors [12].

- Human BR: The typical resting BR for humans ranges between 12 to 20 breaths per minute, with deviations attributable to age, activity level, and health conditions [99].

- Cat BR: Cats exhibit a resting BR range of 11 to 38 breaths per minute, which can narrow to 15 to 31 breaths per minute during sleep [58].

## 3.3   Contact Vital Sign Measuring Devices

Accurate vital sign monitoring has led to the development of various devices, from sophisticated electrocardiograms to wearable sensors like the Polar Belt H10, catering to both human and veterinary medicine.

### 3.3.1   Humans

Advancements in sensor technology have significantly enhanced the accuracy and convenience of human vital sign monitoring:

- Electrocardiogram (ECG): ECGs are the gold standard for heart monitoring, providing comprehensive insights into heart electrical activity [87].

- Polar Belt H10: This chest strap monitor is celebrated for its accuracy, widely used in clinical and research settings for continuous HR monitoring [29, 105].

- Impedance Plethysmography: Though less common, this method measures chest impedance changes with each heartbeat, offering another avenue for vital sign monitoring [18].

### 3.3.2   Animals

Monitoring animal vital signs, especially HR, poses unique challenges, notably due to fur:

- Polar Belt H10: Attempts to use the Polar Belt H10 for cat HR monitoring have shown mixed results, highlighting the potential impact of factors like proximity to other devices and movement on data accuracy [31].

- Polar Verity Sense: While similar in functionality to the Polar OH1, its application for animal HR monitoring remains underexplored due to direct skin contact requirements [71].

- CONTEC08A-VET: Used for blood pressure and pulse rate measurements in various animals, demonstrating the versatility of electronic sphygmomanometers in veterinary settings [16].

- Smartphone-based HR Sensors: Emerging studies indicate the potential of smartphone-based ECG sensors for animal HR monitoring, offering a balance between accuracy and animal comfort [68].

There has been an attempt to use various wearable sensors to monitor HR in cats. However, none of these sensors, with the exception of the gold standard electrocardiogram (ECG) technology, have demonstrated acceptable accuracy. Consequently, measuring the HR of cats without removing fur and attaching electrodes remains a significant challenge.

# Chapter 4

# Radars

## 4.1 A Brief Introduction to Radars

Radars (Radio Detection and Ranging) employ electromagnetic waves to identify and locate objects. By emitting a signal and analyzing its reflection from targets, radars can deduce properties such as distance, speed, and direction. The resolution of a radar system, crucial for distinguishing closely spaced objects, improves with shorter wavelengths ($\lambda$), calculated as $\lambda = \frac{c}{f}$, where $c$ is the speed of light and $f$ is the wave frequency.

## 4.2 MmWave Radars

Operating in the 30 GHz to 300 GHz frequency range, mmWave (millimeter-wave) radars offer high resolution, compactness, and low power consumption. These advantages make them ideal for high-accuracy applications including vital sign detection. The high-frequency operations of mmWave radars necessitate specialized components for signal generation and processing.

A typical mmWave radar system includes:

- **Transmitter:** Utilizes a voltage-controlled oscillator (VCO) for generating the carrier signal.

- **Antenna:** A patch or horn antenna designed for specific radar frequencies.

- **Receiver:** Employs a low-noise amplifier (LNA) and a mixer for signal processing.

- **Signal Processing Unit:** Uses FFT and digital signal processing (DSP) for data analysis.

- **Control Unit:** Manages radar operations using microcontrollers or FPGAs.

MmWave radars have emerged as a non-invasive solution for detecting human vital signs, capable of identifying minute physiological movements. A comparison between the radars can be seen in Figure 4.1 [69].

## 4.3 FMCW Radars

FMCW (Frequency Modulated Continuous Wave) radars emit a continuous signal with linear frequency modulation, allowing simultaneous distance and velocity measurements. Offering higher range resolution and the ability to detect multiple objects, FMCW radars

| Feature | CW | FMCW | UWB-IR | SFCW |
|---|---|---|---|---|
| Long distance detection | x | ✓ | ✓ | ✓ |
| High detection accuracy | ✓ | ✓✓ | ✓✓ | ✓✓ |
| Target speed detection | ✓ | ✓ | ✓ | ✓ |
| Multiple subjects' detection | x | ✓ | ✓ | ✓ |
| Through wall detection | ✓ | ✓✓ | ✓✓ | ✓✓ |
| Localization | x | ✓ | ✓ | ✓ |
| Simplicity | ✓✓✓ | ✓✓ | ✓ | ✓✓ |
| Low cost | ✓✓✓ | ✓✓ | ✓ | ✓✓ |
| Target range | x | ✓ | ✓ | ✓ |
| Tiny motion detection | ✓ | ✓ | ✓ | ✓ |
| High SNR | ✓ | ✓✓ | ✓✓ | ✓✓ |

FIGURE 4.1: Features of different potential radar types for use in vital sign detection [69].
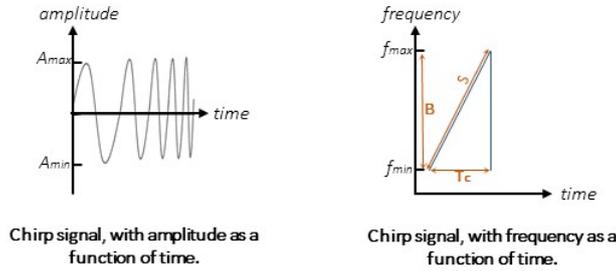


FIGURE 4.2: Chirp signal visualization as amplitude and frequency as a function of time.

excel in vital sign monitoring. The transmitted signal's chirp is critical, typically taking a linear sawtooth waveform for simplicity and efficiency, as visualized in Figure 4.2.

### 4.3.1 Transmitted Signal

The transmitted signal for a single chirp can be expressed by parameters: bandwidth ($B$), start frequency ($f_0$), and duration of the chirp ($T_c$). The slope of the chirp ($S$) indicates the rate of change of frequency and can be calculated as $S = B/T_c$. All these parameters can be adjusted when configuring the radar. Since the chirp is a sinusoid signal whose frequency increases linearly with time, the transmitted chirp in time can be described mathematically as follows:

$$x_t(t) = A_t \sin(\omega_t t + \phi_t), \tag{4.1}$$

where $A_t$ is the amplitude of the transmitted chirp signal, and $\omega_t$ is the angular frequency of the chirp transmitted signal, where $f_0$ is the start frequency:

$$\omega_t = 2\pi(f_0 + St). \tag{4.2}$$

$\phi_t$ is the phase of the transmitted chirp signal, where $R$ is the distance between the radar's antenna and the object [81]:

$$\phi_t = \frac{4\pi R}{\lambda}. \tag{4.3}$$

It is common to also express radar signals using the exponential domain representation as follows [23]:

$$x(t) = e^{j\theta} = e^{j(2\pi f_0 t + \pi St^2 + \phi_t)}, \tag{4.4}$$

where $f_c$ is the carrier frequency, $t$ is the time within each chirp ramp period such that $0 < t < T_c$. This formula is obtained by starting with Euler's formula $e^{j\theta} = \cos(\theta) + j\sin(\theta)$, which, when applied to Equation 4.1, results in the following formula:

$$x_t(t) = A_t \left[\cos(\omega_t t + \phi_t) + j\sin(\omega_t t + \phi_t)\right]. \tag{4.5}$$

When expanding this trigonometric function using Euler's formula, it results in the following:

$$x_t(t) = A_t \left[e^{j(\omega_t t + \phi_t)} + je^{-j(\omega_t t + \phi_t)}\right]. \tag{4.6}$$

### 4.3.2 Received Signal and Intermediate Frequency Signal

After the chirp signal has been transmitted, it is reflected by an object in its path back to the receive antenna of the radar. The received signal differs in phase and angular frequency. The transmitted and received signals are then fed to an electronic component called a mixer, which creates a new signal from the two called the intermediate frequency (IF). The mixer multiplies the signals over time, where the mathematical product of two sinusoids results in a sum of two components. The IF signal contains the frequency and phase difference between the transmitted and received chirp signals, which can be found once the received signal $x_r(t) = A_r \sin(\omega_r(t - t_d) + \phi_r)$ is mixed with the transmitted signal $x_t(t)$ in the time-domain representation using Euler's formula:

$$x_{IF}(t) = A_{IF} \sin\left(2\pi(f_0 + St)t - 2\pi f_b(t - t_d) + \phi_t - \phi_r\right), \tag{4.7}$$

where $\omega_r(t) = 2\pi f_b(t - t_d)$ is the angular frequency of the chirp received signal, $f_b$ is the received beat frequency, $A_r$ is the amplitude of the received chirp signal, and $\phi_t$ is the phase of the received chirp signal. $t_d$ is the delayed time of the transmitted chirp signal and can be calculated as follows:

$$t_d = \frac{2R}{c}. \tag{4.8}$$

The initial phase $\phi_0$ of the IF signal is the difference between the phase of the transmitted and received signals:

$$\phi_0 = \phi_t - \phi_r = 2\pi f_0 t_d. \tag{4.9}$$

The initial IF signal also contains unwanted mixer products and out-of-band signals in the form of high frequency, which are filtered by a low-pass filter within the radar and hence will not be used further [81]. The explained proceeds so far is visualized in Figure 4.3.

When expressing the IF signal using exponential representation:

$$x_{IF}(t) = A_{IF} \left[e^{j(2\pi(f_0 + St)t - 2\pi f_b(t - t_d) + \phi_0)} - e^{-j(2\pi(f_0 + St)t - 2\pi f_b(t - t_d) + \phi_0)}\right]. \tag{4.10}$$

### 4.3.3 ADC Sampling

After the transmitted and received signals are mixed and the IF signal is obtained, this IF signal (Equation 4.7) is sampled by the ADC, which quantizes the signal in time and amplitude. The ADC sample time corresponds to the time quantization, and the ADC bit amount determines the amplitude quantization. The sampling seed of the ADC needs to
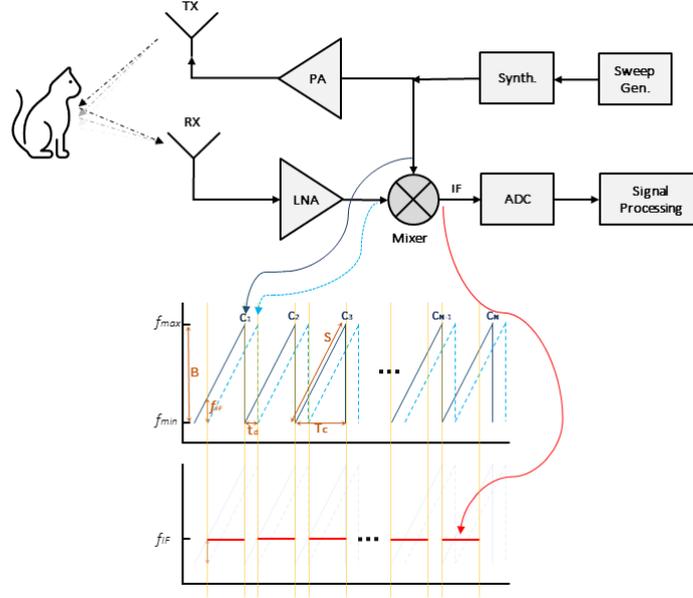
FIGURE 4.3: Simplified working principle of a FMCW radar.

be determined based on the IF and its bandwidth. The sampled IF signal can be written as follows [101]:

$$x_n[n] = A_{IF} \sin \left[ (\omega_t(nt_s) - \omega_r(nt_s)) \, nt_s + \phi_t(nt_s) - \phi_r(nt_s) \right], \tag{4.11}$$

where $t_s = 1/F_s$ is the sampling time, and $n = 0, 1, ..., N_D - 1$ are the total samples, where $N_D$ is the total amount of samples.

## 4.4 Research Question 1 Answered

Reflecting on the research question, "How does FMCW radar technology operate, and why is it suitable for non-invasive monitoring of vital signs such as HR and BR in humans and animals?" the chapter underscores that FMCW radar operates by emitting a continuous wave that is frequency-modulated. This method is adept at detecting minute changes in frequency and phase, which correlate with the displacement caused by human and animal vital signs. The suitability of FMCW radar for non-invasive monitoring lies in its high resolution and sensitivity to small movements, essential for capturing the subtle chest displacements associated with HR and BR. Moreover, the adaptability of chirp parameters allows the radar to be fine-tuned for different subjects, making it a versatile tool for vital sign detection across species.

# Chapter 5

# Hardware Overview

This chapter briefly compares mmWave FMCW radars utilized in various studies, emphasizing the selection of the Texas Instruments AWR1642 radar for this project due to its suitability for vital sign detection and activity recognition tasks.

## 5.1 Radar Selection

Among the mmWave FMCW radars, the Texas Instruments (TI) AWR1642 stands out for its balance between transmitter-receiver configuration and integration of digital signal processors (DSPs) and advanced RISC machines (ARMs), making it an ideal choice for this study.

The AWR1642BOOST operates in the 77 GHz to 81 GHz frequency band, featuring an integrated antenna array for wide field-of-view detection. Its single-chip solution combining RF and DSP components facilitates a compact design, crucial for applications requiring high range and Doppler resolution. The DCA1000EVM serves as an interface between the radar sensor and a computer, enabling efficient raw data acquisition and visualization. It supports high-speed data transfer, ensuring seamless capture and processing of raw radar data for in-depth analysis.

## 5.2 Optimal Radar Configuration

### 5.2.1 Key Configuration Parameters for Vital Sign Detection

For accurate vital sign detection, the radar configuration focuses on optimizing parameters for precision in range and velocity measurement:

- **Chirps per Frame:** Multiple chirps per frame enhance the radar's ability to detect velocity changes, aiding in the differentiation of various activities.

- **Frame Period:** The frame period affects data acquisition speed, with a shorter frame period enabling quicker updates and detection of rapid movements.

- **Sweep Bandwidth:** A wider sweep bandwidth allows for finer range resolution, critical for distinguishing small displacements caused by heartbeat and breathing.

- **Sampling Rate:** A higher sampling rate ensures a detailed capture of the signal, essential for detecting subtle physiological movements.

### 5.2.2 Key Configuration Parameters for Activity Recognition

For AR, the optima radar configuration is slightly different. Given the project's focus on detecting subtle movements of pets, the configuration is tailored to maximize velocity resolution while balancing computational complexity:

- **Chirps per Frame:** A high number of chirps per frame is selected to improve velocity resolution, crucial for identifying fine movements such as those in animal activity recognition.

- **Frame Period:** The frame duration is optimized to ensure an adequate number of chirps within each frame, balancing between velocity resolution and frame rate.

- **Sweep Bandwidth:** The full bandwidth is utilized to maximize range resolution, aiding in the precise detection of distance and movement characteristics.

The configuration settings chosen for this project prioritize accurate detection of subtle movements, essential for the successful monitoring of vital signs and recognition of animal activities.

# Chapter 6

# Vital Sign Signal Processing

Due to the numerous signal processing methods for HR and BR estimation, a dedicated chapter is presented to describe the pre-processing of the data and the various methods for HR and BR estimation.

## 6.1 Pre-processing

After obtaining the ADC data, as described in Section 4.3.3, it can be further read from a file to execute vital sign signal processing steps discussed in the next sections.

### 6.1.1 FFT

The beat frequency $(f_b)$ in the IF signal indicates the target's range due to its relation to the time delay $(t_d)$, reflecting the object's distance. The formula for calculating $f_b$ is:

$$f_b = \frac{2SR_0}{c} \tag{6.1}$$

where $R_0$ is the target's range, showing $f_b$'s dependency on distance. The Range FFT, applying a FFT on the IF signal to move it to the frequency domain, isolates range information by representing different ranges as peaks. The corresponding range $R(f)$ for a frequency $f$ in the FFT output is given by:

$$R(f) = \frac{c}{2S(f - f_b)} \tag{6.2}$$

This process decomposes the signal into frequency components, each tied to a specific range bin, with the FFT's range bins determining the range resolution. The choice of range bin size is crucial for accurate target detection and tracking. The Short-Time Fourier Transform (STFT) analyzes time-segmented signal chunks using the FFT, accommodating the heart waveform's time-varying nature. It is executed by sliding a window of length $M$ across the signal, calculating the DFT for each segment with an overlap of $L$ samples to mitigate signal attenuation at window edges. The segment count $K$ is determined by:

$$K = \frac{N_x - L}{M - L} \tag{6.3}$$

### 6.1.2 Clutter Removal

Clutter removal is critical for isolating the target signal from environmental interference. This process typically involves subtracting the average value from each range bin to eliminate static background signals. A moving average filter, which computes the mean within a sliding window, is instrumental in smoothing signals and attenuating high-frequency noise. According to [45], employing a moving average filter following a differential operation effectively mitigates disruptions from environmental and hardware sources. Similarly, [35] demonstrates the application of such a filter to purify the unwrapped phase signal, showcasing its utility in enhancing signal clarity and reducing noise.

### 6.1.3 Range Bin Selection (Target Detection)

Range bins, divisions along the radar's radial distance, are crucial for determining the range interval of detected objects. The resolution of these bins, and thereby the precision in object detection, is directly influenced by the IF signal length, which in turn depends on the bandwidth. The relationship between range resolution $R_{res}$ and bandwidth $B$ is given by:

$$R_{res} = \frac{c}{2B} \tag{6.4}$$

A 4 GHz bandwidth, for instance, yields a 3.75 cm range resolution, adequate for capturing human chest displacement within a single range bin due to its minor amplitude during breathing [89]. Opting for a smaller bandwidth increases range bin width, simplifying signal processing by encompassing entire chest displacements in fewer bins [28]. However, bandwidth reduction narrows the frequency range for noise susceptibility, potentially increasing noise impact [80], [9].

Moreover, FMCW radar's range accuracy is affected by phase noise and frequency ramp non-idealities, impacting signal phase and magnitude, hence influencing range detection [11]. Nonlinearity in frequency ramps complicates accurate range measurement, necessitating multiple range bin analyses for precise target detection [9].

### 6.1.4 DC Offset Correction

DC offset correction is pivotal for phase extraction, mitigating nonlinear distortion and false target detections by removing overlaid external DC components and addressing local oscillator leakage and signal mixer non-linearity [111]. It also counters issues like Tx-Rx antenna leakage, cross-talk, stationary clutters, and phase modulation from vibrating objects, which contribute to DC presence [24, 119, 54]. The received signal encompasses both stationary clutters and the target's motion, necessitating DC compensation for accurate phase analysis [9].

Radar signals comprise in-phase (I) and quadrature (Q) components, representing the real and imaginary parts of the signal, respectively. The complex signal $x(t)$ and its amplitude $A(t)$ and phase $\phi(t)$ are described by:

$$x(t) = \Re(t) + j\Im(t) = A(t)e^{j\phi(t)}, \tag{6.5}$$

Adjusting for DC offset, the phase becomes:

$$\phi(t) = \arctan\left(\frac{\Im(t) + dc_q}{\Re(t) + dc_i}\right), \tag{6.6}$$

where $dc_q$ and $dc_i$ are the DC components of the imaginary and real parts, essential for retaining displacement information.

DC correction methods include circular center dynamic tracking and nonlinear least squares estimation (NLLS), aiming to recalibrate the signal's complex plane origin [111, 61, 9].

**NLLS Algorithm:** Proposed in [9], NLLS estimates the signal cloud's center and radius by minimizing:

$$P = \min_{x,r} \sum_{i=1}^{N} \left(||x - a_i||^2 - r^2\right)^2, \tag{6.7}$$

where $a_i$ is the $i$-th sample, $x$ the circle's center, and $r$ its radius.

**Gradient Descent Algorithm:** Employing a gradient descent algorithm for DC offset correction dynamically adjusts I/Q channels. It optimizes:

$$P(dc_i, dc_q, A_R) = \min \sum_{i=1}^{N} \left(\sqrt{(I[i] - dc_i)^2 + (Q[i] - dc_q)^2} - A_R\right), \tag{6.8}$$

where $dc_i$ and $dc_q$ are the DC offsets for I and Q signals, and $A_R$ the amplitude, ensuring precise DC adjustment [62].

### 6.1.5 Phase Analysis

Phase analysis is paramount in mmWave sawtooth radar for HR and BR estimation, crucial when chest movements are subtle ($< 1$ mm) and beyond the 3.75 cm maximum range resolution's capability for vital sign detection. This necessitates using beat frequency exclusively for range estimation to pinpoint the target, with phase changes in the reflected signal indicating chest movement. The IF signal comprises real and imaginary components, with the real part expressed as a cosine function and the imaginary part as a sine function:

$$\Re\{x_{IF}(t)\} = A_{IF} \cos(2\pi(f_0 + St)t - 2\pi f_b(t - t_d) + \phi_t - \phi_r),$$

$$\Im\{x_{IF}(t)\} = A_{IF} \sin(2\pi(f_0 + St)t - 2\pi f_b(t - t_d) + \phi_t - \phi_r).$$

**Arctan:**

The phase $\phi(t)$ is derived using the arctangent function to elucidate the signal's time-dependent angular component:

$$\phi(t) = \arctan\left(\frac{\Im\{x_{IF}(t)\}}{\Re\{x_{IF}(t)\}}\right). \tag{6.9}$$

Essential for HR and BR estimation, phase unwrapping corrects discontinuities by adjusting phase jumps beyond $\pm\pi$, ensuring a coherent phase trajectory. This process

is vital for representing the phase accurately, facilitating precise velocity and distance measurements in radar applications.

Phase unwrapping modifies phase jumps exceeding $\pi$ to their $2\pi$ equivalent, maintaining a continuous phase sequence crucial for dependable signal analysis in radar systems.

**DACM:**

While arctangent phase calculation is generally effective, its direct application is limited to a native range of $(-\pi/2, \pi/2)$, leading to discontinuities beyond this interval as illustrated in Figure 6.1, particularly in cases of significant demodulation or noise [107].

The Differentiate and Cross-Multiply (DACM) algorithm, avoiding trigonometric calculations, derives the phase change rate $\omega(t)$ as:

$$\omega(t) = \frac{\mathrm{d}}{\mathrm{d}t}\left[\arctan\frac{Q(t)}{I(t)}\right] = \frac{I(t)\dot{Q}(t) - \dot{I}(t)Q(t)}{I(t)^2 + Q(t)^2}, \tag{6.10}$$

effectively circumventing the arctangent function's range limitations and resolving phase discontinuity issues. However, DACM's sensitivity to noise, due to differentiation, poses challenges, especially for low-frequency signals and noise amplification [106, 85].
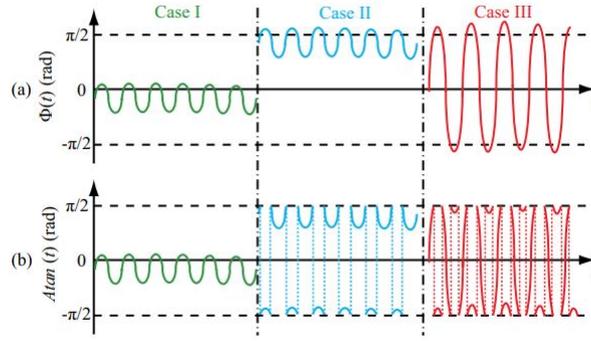


FIGURE 6.1: (a) Desired phase demodulation results and (b) the corresponding arctangent demodulation results. Case I: the vibration amplitude is small and the DC component of the desired result is far from the boundary of $(-\pi/2, \pi/2)$. Case II: the vibration amplitude is small and the DC component of the desired result is close to $\pi/2$. Case III: the vibration amplitude is larger than $\lambda/8$ [107].

**Extended DACM (EDACM):**

EDACM enhances DACM's noise performance by incorporating an accumulator for both low and high-frequency adjustment, represented in the digital domain by:

$$\phi[n] = \sum_{k=2}^{n} \frac{I[k](Q[k] - Q[k-1]) - Q[k](I[k] - I[k-1])}{I[k]^2 + Q[k]^2}, \tag{6.11}$$

where continuous operations are discretized, mitigating the original DACM's limitations and improving noise handling [107].

### 6.1.6 Phase Difference

The application of phase difference operations significantly enhances data quality by amplifying the heartbeat signal and streamlining its extraction. This method has been successfully applied to accentuate heartbeat components but introduces impulse noise as a

side effect [104, 112]. Such noise can be effectively mitigated using filtering techniques, with the median filter being a notable example for its efficacy in removing impulse noise [115]. The differential phase, representing the variance between sequential phase readings, is straightforwardly computed as $\phi[n] - \phi[n-1]$, simplifying signal processing efforts for vital sign detection.

## 6.2 Filtering

Filtering techniques refine the extracted phase signal by removing noise and extraneous components, tailoring the signal for vital sign (HR and BR) estimation without directly estimating these parameters.

**Median Filter:** A median filter, which replaces each data point with the median of its neighbors, effectively removes noise while preserving signal edges. It's applied pre- or post-phase extraction to mitigate impulse noise, preparing the signal for further processing with BPF and FFT for HR and BR estimation [30, 115].

**Moving Average (MA) and Weighted Filters:** MA filters smooth signals by averaging adjacent points, while Weighted Moving Average (WMA) and Exponentially Weighted Moving Average (EWMA) filters offer nuanced control over emphasizing recent data or specific signal characteristics, crucial for noise reduction and highlighting vital sign indicators in radar signal processing.

**Band-Pass Filter (BPF):** BPF isolates the frequency band pertinent to vital signs, reducing noise and interference. For humans, frequencies typically range from 0.1Hz to 0.9Hz for BR and 0.6Hz to 4.2Hz for HR, with subsequent peak detection or advanced methods for estimation [57, 104, 97].

**Butterworth and FIR Filters:** Butterworth filters, known for their smooth passband response, and FIR filters, prized for linear phase characteristics, are employed post-median filtering or on raw phase data. These filters, with carefully chosen passbands, enhance the signal's clarity for vital sign detection [115, 63].

## 6.3 After Filtering

### 6.3.1 FFT

Fourier Transform (FT) analysis on the phase signal distinguishes frequencies, aiming to identify HR and BR. Despite challenges like motion artifacts and environmental noise, FT effectively detects BR due to its larger amplitude. However, HR detection, marked by subtler chest movements, often necessitates additional processing for accuracy [30, 97]. The Chirp Z-Transform (CZT) enhances frequency spectrum analysis, offering refined resolution beneficial for HR extraction [112]. Similarly, Short-Time FT (STFT) divides the signal into segments for detailed frequency analysis [30].

Spectral leakage and limited frequency resolution ($f_r = F_s/N$) due to non-periodicity pose challenges in using FT. With a typical resolution of 1 bpm, errors can be significant, especially for BR as low as 3 bpm. CZT addresses resolution limitations, offering improved analysis, and so does zero padding and Rife algorithm.

**Zero Padding:** Zero padding, by interspersing zeros before FFT, interpolates the signal, enhancing frequency resolution [113]. This technique expands the time window ($T_w$), reducing frequency spacing ($f_r = 1/T_w$) between FFT bins and achieving finer spectral detail.

### 6.3.2 Other Filters

The Kalman filter, a recursive algorithm for dynamic system state estimation, enhances SNR by filtering in-band noise, improving waveform quality. It is utilized after a band-pass filter (BPF) for heartbeat 3rd harmonics and heartbeat extraction, with initial HR values obtained through peak-to-valley differences and Rife algorithm application [45, 19]. Peak detection algorithms identify vital sign signal peaks, corresponding to heartbeats for HR and inhalation/exhalation for BR. Techniques range from threshold-based to wavelet transform-based methods, with peak-valley pairs aiding in eliminating noise-induced peaks for accurate HR estimation [57, 45]. CZT, offering superior frequency resolution over standard FFT, is crucial in analyzing non-uniformly sampled signals or those with variable frequencies, through its capability to interpolate signals in the frequency domain. Employed for precise frequency estimation, the Rife algorithm iteratively refines spectral peak estimations, crucial for accurate HR and BR detection post-FFT. This method has seen application alongside Kalman filters and FFT to improve HR estimation accuracy [19, 118, 20, 17]. Wavelet transform methods, such as CWT and DWT, offer time-frequency domain analysis, enabling transient event localization and frequency-specific information extraction for HR and BR analysis [39].

# Chapter 7

# Human Vital Sings

In this chapter, the implementation steps and results of human vital sign detection are detailed. Background information, methodology, participant details, data collection scenarios, experimental setup, and data acquisition can be found in Appendix A, which presents an article about the dataset recorded for this thesis. The data analyzed in this chapter were collected from Participants 2, 3, 4, and 6. As described in Appendix A, Participant 2 exhibits comparatively lower heart and breathing rates, attributable to their experience with meditation. Conversely, Participant 6 has higher rates, which can be attributed to their asthma condition. The objective is to analyze data from participants with diverse physiological profiles to account for real-world scenarios and potential user applications.

## 7.1 Implementation and Testing

### 7.1.1 Overview

The block diagram illustrating the steps involved in signal processing for vital signs detection is presented in Figure 7.1. The implementation is divided into three parts, where the first part different DC offset correction methods are compared, in the second part different phase calculation methods are compared, and in the third part three methods for detecting HR and BR against a reference sensor are compared. The methods are: peak counting, FFT, and the Rife Algorithm combined with FFT. Subsequent sections will delve into each component of the diagram in greater detail.
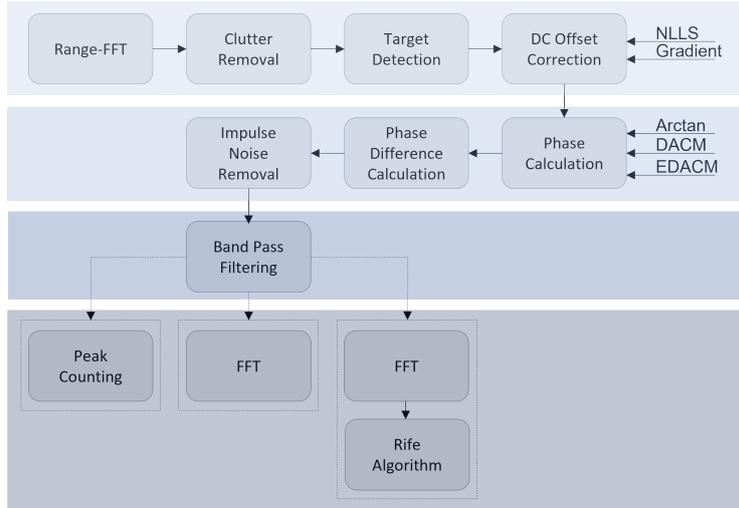
FIGURE 7.1: Block diagram illustrating the simplified process for detecting HR and BR.

## 7.1.2 Data Processing

In the following sections, each signal processing block is described in detail, accompanied by example results for each block. The data used for illustration is derived from participant 4 in the first distance scenario of the third measurement, where the distance between the participant's chest and the radar is approximately 40 cm.

**Range-FFT**   The spectrogram generated by the Range-FFT process illustrates how the energy distribution across various range bins evolves over time. This visualization is particularly valuable for tracking movements of targets or detecting changes within the radar's observed scene. As can be seen in Figure 7.2, a significant portion of the energy is concentrated within a single range bin, indicating the location of the primary target.
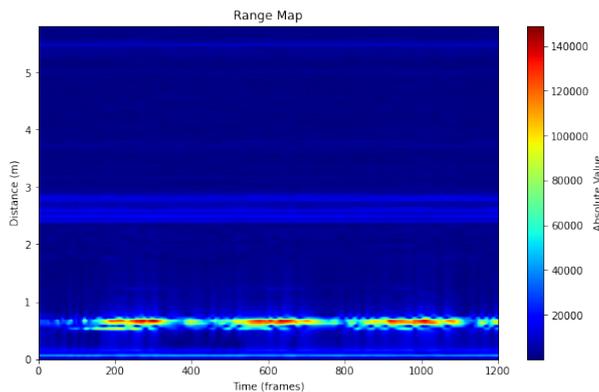


FIGURE 7.2: Spectrogram from Range-FFT showing the distribution of energy across range bins over time.

**Clutter Removal**   The clutter removal is removing all the static objects by calculating the average value for each range bin and then removing the mean value for each of the range bins (Figure 7.3).
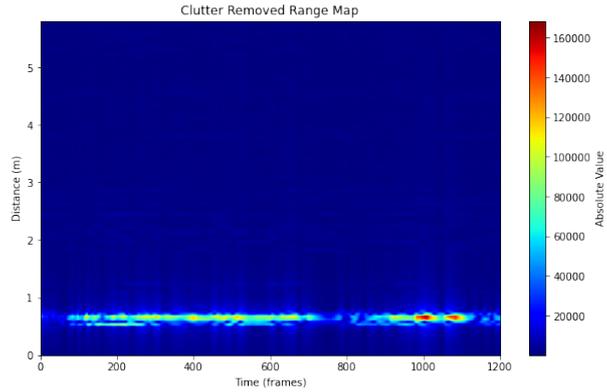
FIGURE 7.3: Spectrogram from Clutter Removed Range-FFT showing the distribution of energy across range bins over time when the static clutter signal is removed.

**Target Detection** After clutter removal, the next step involves processing the range-FFT data to identify a specific target range bin. This is done by calculating the frequency with which each range bin achieves the maximum value across all frames. By analyzing the absolute values of the FFT data, the range bin that most frequently contains the maximum value is pinpointed as the target's location. As illustrated in Figure 7.4, range bin 14 was identified as the target location in 786 out of 1200 frames, among 250 total range bins. This selection is critical for subsequent signal processing steps. Figure 7.5 shows the range profile for all frames, highlighting the dominance of range bin 14 and explaining the frequent occurrence of adjacent bins like 13 due to their proximity.

```
Counts of max occurrences per range bin: [  0   0   0   0   0   0   0   0   0   0   0  87  26 272 786  28   1]
Descending order of occurrence counts for range bins: [14 13 11 15 12 16  5  1  2  3  4  8  6  7  9 10  0]
Most occurring range bin: 14
```

FIGURE 7.4: Occurrences of target range bin across frames.
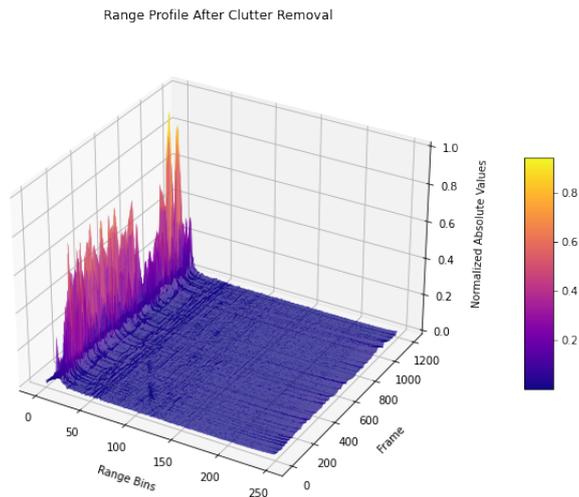


FIGURE 7.5: 3D range profile showing FFT values across frames.

**DC Offset Correction** This step involves correcting the DC offset in FFT data using a Nonlinear Least Squares (NLLS) algorithm. The process estimates and then subtracts

the offset, aiming to center the data around the origin on the complex plane. The plot in Figure 7.6 shows both the original and corrected data. Additionally, the estimated centers of the data before and after correction are marked to validate the adjustment. Although the center estimate post-correction is nearly at zero, the NLLS method results in a slight positive shift. This deviation is supposed to illustrate the relative accuracy of NLLS compared to simple mean-based center estimation.
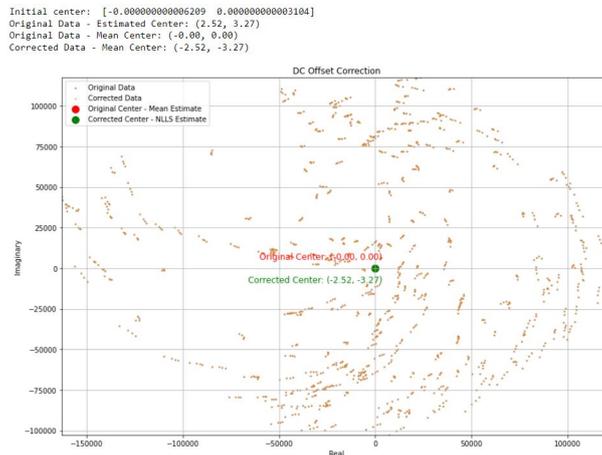


FIGURE 7.6: Comparative scatter plot showing DC offset correction.

**Phase Calculation** The EDACM algorithm is employed to track the phase evolution within FFT data of radar signals. It calculates the phase incrementally, accounting for variations in the real and imaginary parts of the signal between successive samples. This approach enables the visualization of phase changes over time, as shown in Figure 7.7. Furthermore, EDACM unwraps the phase, allowing for a representation of continuous phase evolution without the limitations of $2\pi$ wrapping, ensuring the phase can increase or decrease unbounded.
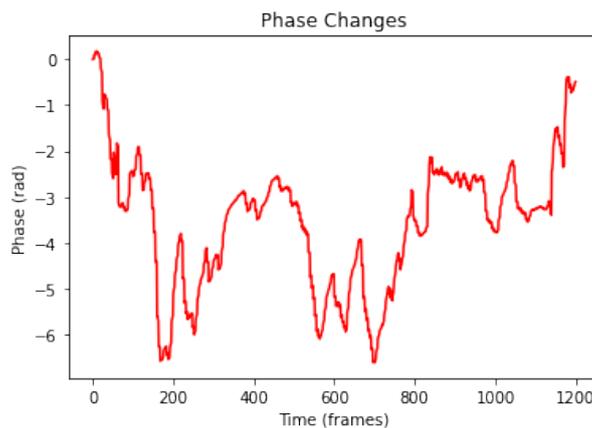


FIGURE 7.7: Continuous phase evolution over time, using EDACM.

**Phase Difference Calculation** The phase difference represents the variation in phase between consecutive samples, determined by calculating the numerical difference of the unwrapped phase data. This calculation highlights temporal phase changes due to chest displacement, enhancing the detection of periodic movements from heartbeats and respira-

tion. As shown in Figure 7.8, notable spikes are observed. These spikes are not attributed to heartbeats or breathing, which would typically manifest as regular, smaller fluctuations in line with the heartbeat rhythm. Instead, the large spikes are indicative of significant movements or impulse noise which is disrupting the expected pattern.
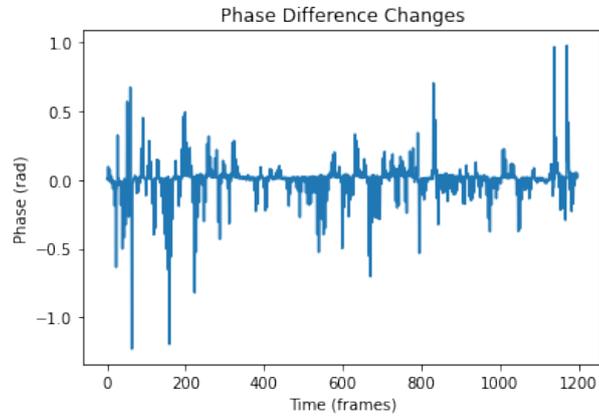


FIGURE 7.8: Identifying temporal changes and noise through phase difference.

**Impulse Noise Removal**  Selective filtering is employed to eliminate impulse noise, applying a median filter selectively to outliers significantly deviating from their neighboring values, based on a set threshold. This method specifically targets and mitigates noise spikes, thereby smoothing them out, without distorting the signal's overall integrity and preserving the signal features critical HR and BR detection. Figure 7.9 demonstrates the effect of this filtering, particularly on the largest spikes. The illustration is confined to 600 of the total 1200 frames to enhance the visibility of the noise spikes' details.
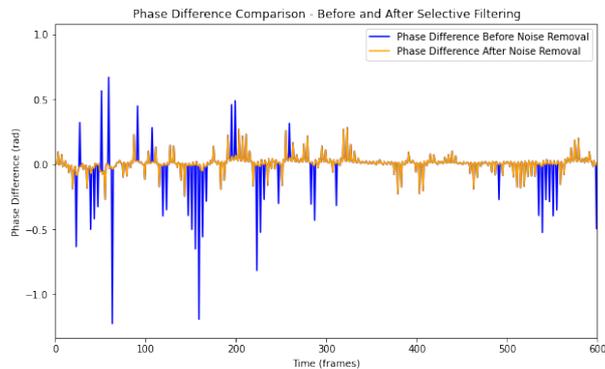


FIGURE 7.9: Selective filtering smoothing out large noise spikes over 600 frames.

**Band Pass Filter**  To isolate the frequencies relevant to BR and HR, two band pass filters are employed. One filter is applied to retain only the frequency range associated with BR (0.07 - 0.4 Hz), while the other focuses on the frequency range pertinent to HR (1 - 1.5 Hz). This filtering process effectively removes unrelated frequency components, sharpening the focus on the signals of interest.
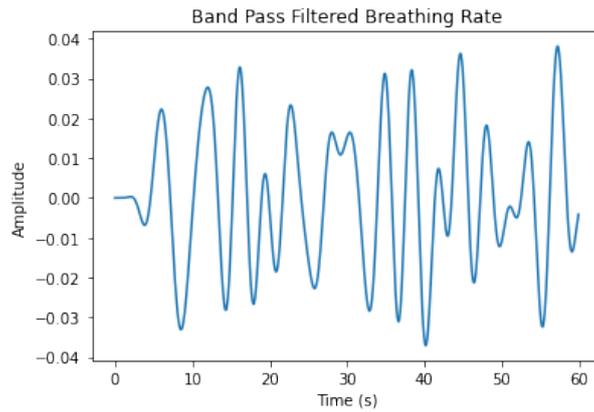
FIGURE 7.10: Filtered breathing rate signal, highlighting BR frequency components.
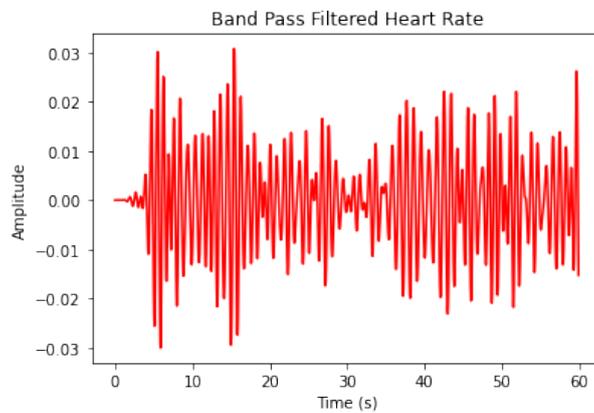


FIGURE 7.11: Filtered heart rate signal, emphasizing HR frequency components.

**FFT** As indicated in the block diagram (Figure 7.1), the initial step involves employing the FFT to identify the dominant frequency within the signal. To enhance the FFT's resolution from 0.0167 Hz to 0.0056 Hz, equivalent to an accuracy of 0.33 bpm, zero-padding is applied before the FFT process. Figures 7.12 and 7.13 showcase the frequency plots for the breathing and heart rates, respectively, before and after applying zero-padding, along with the identified dominant frequency.

FFT of BR is 0.21684737281067556Hz x 60 = 13.011 BPM at frequency index 13.
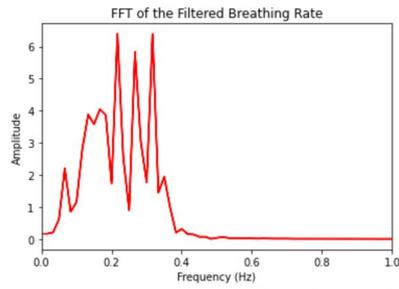


FFT of BR is 0.21684737281067554Hz x 60 = 13.011 BPM at frequency index 39.
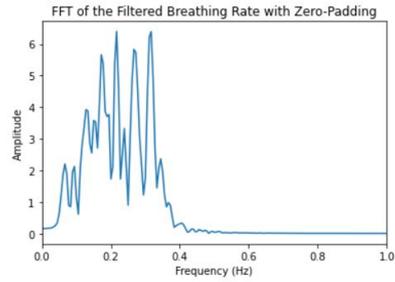


FIGURE 7.12: Breathing rate FFT analysis before and after zero-padding.

FFT of HR is 1.2176814011676396Hz x 60 = 73.061 BPM at frequency index 73.
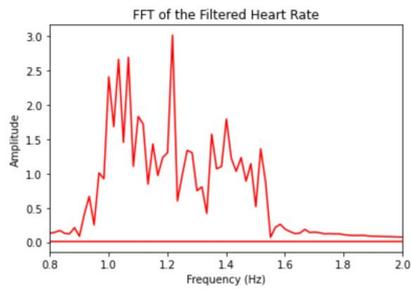


FFT of HR is 1.212121212121212Hz x 60 = 72.727 BPM at frequency index 218.
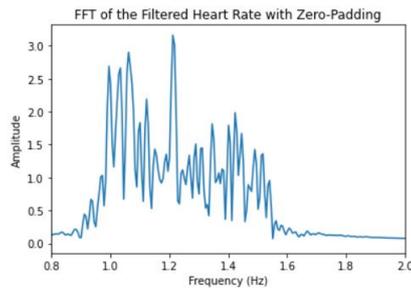


FIGURE 7.13: Heart rate FFT analysis before and after zero-padding.

Following the estimation of HR and BR by radar and their comparison with reference values, the Mean Absolute Error (MAE) is calculated, with the resulting error rates for HR and BR being 9.86% and 7.07%, respectively, as shown in Figure 7.14.

```
Method: FFT
Distance: 40cm
Recording number: 4.1.3

HEAR RATE:
The average reference HR calculated from 0 to 60 seconds: 66.2 BMP
Radar Estimated HR: 72.73
MAE for HR: 6.53 BPM
Error Percentage for HR: 9.86%

BREATHING RATE:
The reference BR counted from 0 to 60 seconds: 14 BPM
Radar Estimated BR: 13.01 BPM
MAE for BR: 0.99 BPM
Error Percentage for BR: 7.07%
```

FIGURE 7.14: MAE and error rates for HR and BR using FFT.

**Rife Algorithm**   The Rife Algorithm enhances frequency estimation accuracy by examining neighboring frequency bins around the peak FFT output. This approach is particularly beneficial when the peak frequency lies between bins—a frequent occurrence with discretely sampled data. By interpolating between these bins, the Rife Algorithm refines the FFT's frequency estimates, theoretically offering a more precise peak frequency determination. Despite the minimal differences observed when comparing the Rife Algorithm's outcomes with those of FFT, the Rife Algorithm is expected to provide superior accuracy. Figures 7.15 and 7.16 showcase the MAE, error percentages, and frequency plots derived from the Rife Algorithm's application to HR and BR data.

```
Method: Rife
Distance: 40cm
Recording number: 4.1.3

HEAR RATE:
The average reference HR calculated from 0 to 60 seconds: 66.2 BMP
Radar Estimated HR: 72.89
MAE for HR: 6.69 BPM
Error Percentage for HR: 10.11%

BREATHING RATE:
The reference BR counted from 0 to 60 seconds: 14 BPM
Radar Estimated BR: 12.86 BPM
MAE for BR: 1.14 BPM
Error Percentage for BR: 8.16%
```

FIGURE 7.15: Error analysis for HR and BR using the Rife Algorithm.
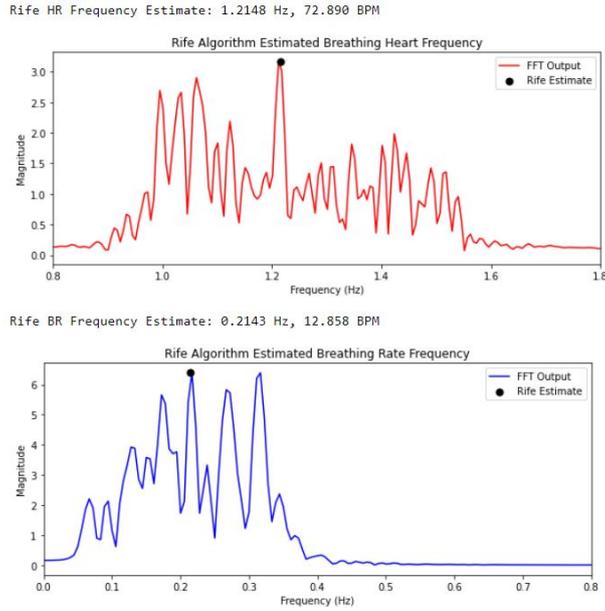
FIGURE 7.16: Frequency analysis for HR and BR with the Rife Algorithm.

**Peak Counting**   Peak Counting is a more straightforward method than both the Rife Algorithm and FFT. Unlike FFT, which analyzes the frequency spectrum to identify the dominant frequency indicative of heart rate, Peak Counting simply tracks the temporal occurrence of peaks within the signal. This technique is particularly useful for direct observation of heart rate and breathing rate through peak events. Figures 7.17 and 7.18 display the detected peaks for BR and HR, respectively, while Figure 7.19 provides the error parameters derived from this method. The threshold is set to be 0.
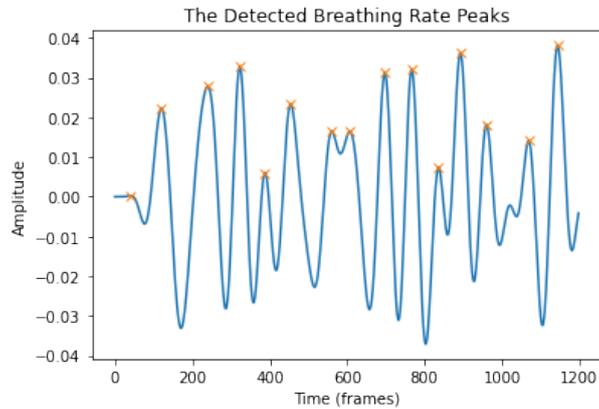


FIGURE 7.17: Plot with the detected peaks of the breathing rate (BR).

41
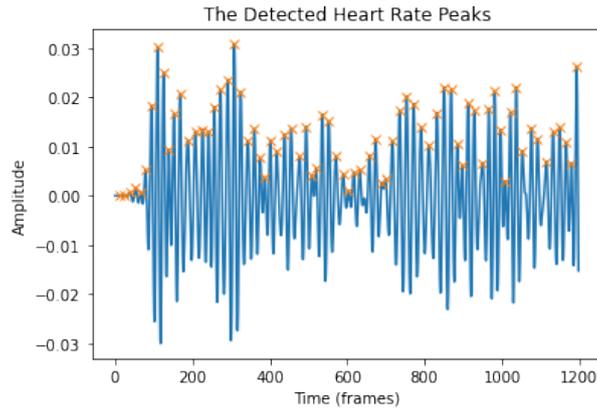
FIGURE 7.18: Plot with the detected peaks of the heart rate (HR).

```
Method: Peak Counting
Distance: 40cm
Recording number: 4.1.3

HEAR RATE:
The average reference HR calculated from 0 to 60 seconds: 66.2 BMP
Radar Estimated HR: 73.06
MAE for HR: 6.86 BPM
Error Percentage for HR: 10.36%

BREATHING RATE:
The reference BR counted from 0 to 60 seconds: 14 BPM
Radar Estimated BR: 15.01 BPM
MAE for BR: 1.01 BPM
Error Percentage for BR: 7.23%
```

FIGURE 7.19: MAE and error percentage for HR and BR using Peak Counting.

## 7.2 Results

The results are divided into three sections, where, in the first section, two different DC offset methods and no method are compared, and then three different phase calculation methods are compared. The most accurate DC offset correction and phase calculation method is chosen. In the third part, three different HR and BR methods are compared.

The metrics used for this analysis include the Mean Absolute Error (MAE) and Mean Error Percentage (MEP). MAE is measured in beats per minute (BPM) for HR and breaths per minute (BPM) for BR, indicating the average absolute error from the reference values. MEP, on the other hand, represents the error as a percentage of the reference values, providing an insight into the relative accuracy of the measurements. Since beats and breaths per minute are translated the same way to Hz, the BPM indication is used for HR and BR.

### 7.2.1 Implementation 1 - DC Offset Correction

AData from 4 participants is used in distances 40 cm and 80 cm, where a single recording is processed per participant, and the average error is calculated across all the used data per used method. When stationary clutters are present at the range of interest, DC compensation is required for the phase analysis, otherwise removing them does not improve the phase quality. As can be seen in Table 7.1, for the used data, there is no difference between the DC offset correction methods. Yet, it is challenging to know if there is any DC offset without testing it.

Table 7.1: Heart Rate and Breathing Rate Error Estimations for Humans at 40 cm and 80 cm Distance by Using Different DC Offset Correction Methods.

| Method | MAE HR (bpm) | MEP HR (%) | MAE BR (bpm) | MEP BR (%) |
|---|---|---|---|---|
| NLLS | 8.26 | 11.27 | 7.34 | 63.21 |
| Gradient | 8.26 | 11.27 | 7.34 | 63.21 |
| Nothing | 8.26 | 11.27 | 7.34 | 63.21 |

### 7.2.2 Implementation 2 - Phase Calculation

gain, data from 4 participants is used in distances 40 cm and 80 cm, where a single recording is processed per participant, and the average error is calculated across all the used data per used method. As can be seen in Table 7.2, the best best performance for HR estimation is by using arctangent method, however, EDACM shows average performance and significantly better performance for BR estimation, hence EDACM is chosen for further processing.

Table 7.2: Heart Rate and Breathing Rate Error Estimations for Humans at 40 cm Distance by Using Different Phase Calculation Methods.

| Method | MAE HR (bpm) | MEP HR (%) | MAE BR (bpm) | MEP BR (%) |
|---|---|---|---|---|
| Arctangent | 8.24 | **10.7** | 12.0 | 123.07 |
| DACM | 11.17 | 14.24 | 8.17 | 87.63 |
| EDACM | 9.16 | 12.1 | 5.67 | **34.98** |

### 7.2.3 Implementation 3 - HR and BR Estimation

This section discusses data processing for 4 participants, each with 4 measurements, to compare three methods for vital sign estimation: FFT, the Rife Algorithm, and peak counting. The radar-estimated HR and BR values are compared to reference values. The Rife Algorithm yields the most accurate estimations for HR and an average BR at a distance of 40 cm, as detailed in Table 7.3. A similar performance is observed for measurements taken at a distance of 80 cm (Table 7.4), where the Rife Algorithm demonstrates superior HR estimation accuracy as FFT. However, FFT outperforms the Rife Algorithm at this greater distance in BR estimation.

Table 7.3: Heart Rate and Breathing Rate Error Estimations for Humans at 40 cm Distance.

| Method | MAE HR (bpm) | MEP HR (%) | MAE BR (bpm) | MEP BR (%) |
|---|---|---|---|---|
| Peak Counting | 7.81 | **10.71** | 8.13 | 102.44 |
| FFT | 9.31 | 12.24 | 7.9 | 72.9 |
| Rife | 8.74 | 11.44 | 6.73 | **49.29** |

TABLE 7.4: Heart Rate and Breathing Rate Error Estimations for Humans at 80 cm Distance.

| Method | MAE HR (bpm) | MEP HR (%) | MAE BR (bpm) | MEP BR (%) |
|---|---|---|---|---|
| Peak Counting | 4.88 | 6.91 | 7.51 | 116.0 |
| FFT | 3.98 | **5.31** | 6.92 | **61.43** |
| Rife | 3.98 | **5.31** | 7.0 | 63.59 |

Observing the method's robustness across diverse physiological profiles highlights variable BR errors, considering the participant 2 with low breathing rate (4 - 6 bpm) and participant 6 with high breathing rate (19 - 22 bpm). For example, MEP BR errors for participant 2 significantly exceed those of other participants, as can be seen in table 7.5. Despite this, HR errors remain consistent across participants. Interestingly, the comparison or errors between participants reveals peak counting algorithms effectiveness in HR and BR estimation across the board, though participant 2's MEP BR error significantly impacts overall performance, hence, significantly increasing the overall error rate.

TABLE 7.5: Heart Rate and Breathing Rate Error Estimations for Humans at 40 cm Distance per Participant with Sum of Errors.

| Participant | Method | AVG MEP HR (%) | AVG MEP BR (%) |
|---|---|---|---|
| 2 | Peak Counting | 22.37 | 1011.17 |
| 2 | FFT | 46.06 | 549.67 |
| 2 | Rife | 33.19 | 174.81 |
| **Sum** | – | **101.62** | **1735.65** |
| **Avg** | – | **33.87** | **578.55** |
| 3 | Peak Counting | 60.96 | 408.18 |
| 3 | FFT | 76.91 | 191.83 |
| 3 | Rife | 77.31 | 187.62 |
| **Sum** | – | **215.18** | **787.63** |
| **Avg** | – | **71.73** | **262.54** |
| 4 | Peak Counting | 72.05 | 78.97 |
| 4 | FFT | 22.58 | 121.7 |
| 4 | Rife | 22.62 | 121.71 |
| **Sum** | – | **117.25** | **322.38** |
| **Avg** | – | **39.08** | **107.46** |
| 6 | Peak Counting | 15.97 | 140.75 |
| 6 | FFT | 50.3 | 303.14 |
| 6 | Rife | 49.84 | 304.54 |
| **Sum** | – | **116.11** | **748.43** |
| **Avg** | – | **38.70** | **249.48** |

This analysis underscores the importance of method selection based on the subject's physiological characteristics and the specific accuracy requirements for HR and BR estimation.

## 7.3 Discussion

The exploration of human vital sign detection through radar technology, particularly for participants with distinct physiological profiles like those experienced in meditation and those with asthma, introduces nuanced challenges and considerations. Including diverse cases such as these is crucial, as it mirrors real-world scenarios where individuals' heart and breathing rates vary significantly due to their physical and mental states. For instance, the need to adjust band pass filters for these unique cases allowed for the passage of harmonics and various noises, which isn't typically accounted for in more standard studies. Specifically, the experienced meditator's data likely saw a large error due to breathing rate harmonics penetrating through the filters, demonstrating the complexities involved in accurately capturing such varied physiological states.

The observation that accuracy is lower for these two particular cases underscores the importance of considering a wide range of physiological conditions in vital signs monitoring. However, it also highlights the potential need for employing different signal processing methods to better accommodate such variations. This realization calls for further exploration into adaptive or more nuanced processing techniques that can dynamically adjust to the specific characteristics of each participant's data, potentially improving the accuracy of heart and breathing rate estimations across a broader spectrum of conditions.

## 7.4 Research Question 2 Answered

Addressing the research question 2, "What signal processing algorithms are necessary for accurately extracting vital sign information (HR and BR) from radar signals?" this section identifies the Rife Algorithm and the EDACM method as key for accurate vital sign extraction. While DC offset correction methods had minimal impact, phase calculation and direct estimation were critical, with the Rife Algorithm excelling in HR accuracy and EDACM in BR accuracy at close range. The study advocates for adaptive signal processing techniques to improve accuracy in diverse physiological conditions, highlighting the need for flexibility in method selection to accommodate variations in human vital signs.

# Chapter 8

# Pet Vital Signs

## 8.1 Methodology

For measuring pets' vital signs, the same radar system and software setup was employed as described in Section 7 and Appendix A, utilizing the AWR1642BOOST and DCA1000.

### 8.1.1 Experiment Setup

The radar system, comprising the AWR1642BOOST and DCA1000EVM, was securely mounted in a microphone holder affixed to an office table. This holder's adjustability facilitated easy modification of the radar's distance from the subject, tailored to each experimental scenario. The pet's bed was positioned directly beneath the radar system and microphone holder, ensuring a consistent location for the pet throughout the experiment. A laptop computer, also placed on this table, facilitated the connection to the radar system, adhering to the procedural guidelines detailed in a specific tutorial [43]. The configuration of this experimental setup is illustrated in Figure 8.1.



FIGURE 8.1: Setup for animal vital sign measurements, showing the radar system positioning above the pet's bed.

### 8.1.2 Distance Scenarios and Data Recording

To evaluate the radar system's efficacy in capturing pets' vital signs, experiments were conducted across four different distances: 65 cm, 40 cm, 30 cm, and 20 cm, measured from the radar antenna to the pet's side. For each distance scenario, six separate recordings were captured. Throughout these sessions, the pet's breaths were meticulously counted and recorded. Additionally, to ensure accuracy and provide a means for verification, a video of each session was captured, allowing for the possibility of recounting breaths if needed.

### 8.1.3 Implementation and Testing

The methodology for implementing and testing the radar system on pets mirrored that used for human subjects, utilizing the same signal processing chain depicted in Figure 7.1. The processing steps followed were identical to those outlined in Section 7.1, ensuring consistency in the analysis of vital signs across different subjects. Thew only differences are that the band pass filter is set for frequencies from 0.37 Hz to 0.74 Hz for BR, and from 1.5 Hz to 2.5 Hz for HR, which is due to higher HR and BR for cats than for humans. The second difference is made in peak counting, where the threshold is set to be 0.1 instead of 0 as for human data processing.

## 8.2 Results

In the following sections, the obtained results are discussed. Firstly, the distance impact on the BR estimations accuracy is discussed, where the average of 4 measurements per distance are used, but for the implementation 1-3, only measurement number 4 is used for each distance, and then the average value of all distances is shown in the Tables accordingly.

### 8.2.1 Distance

In the Table 8.3, results of breathing rate estimation can be seen. Four measurements per distance were processed, where the average errors and heart rate can be seen. The radar system demonstrates potentially improved accuracy for BR measurements at closer ranges (20 cm and 30 cm), yet accuracy does not linearly decrease with increased distance, hinting at other influential factors beyond proximity. Variations in error rates across similar distances underline the significance of the subject's specific conditions and environmental factors on measurement reliability.

TABLE 8.1: Heart Rate Estimations, and Breathing Rate Error Estimations for a Still Cat at Various Distances.

| Method | AVG Estimated HR (bpm) | AVG MAE BR (bpm) | AVG MEP BR (%) |
| --- | --- | --- | --- |
| 20 cm | 105.34 | 4.68 | 14.43 |
| 30 cm | 106.5 | 3.43 | **12.21** |
| 40 cm | 121.27 | 6.59 | 24.8 |
| 65 cm | 115.01 | 8.03 | 32.18 |

### 8.2.2 Implementation 1 - DC Offset Correction

There was not difference between using the difference DC Offset Correction methods, similarly, as it was for human data. More reasoning can be found in Section 7.2.1.

### 8.2.3 Implementation 2 - Phase Calculation

In the Table 8.2, three different phase calculation methods (Arctangent, DACM, and EDACM) were employed. Of these, EDACM shows the best performance in terms of BR errors, with the lowest AVG MAE BR (2.26 bpm) and AVG MEP BR (9.26%). This suggests that EDACM is the most accurate and reliable method for BR estimation among the three, potentially due to its enhanced capability in dealing with noise reduction. In contrast, DACM exhibits the highest BR errors, indicating its relative disadvantage in handling the complexities of phase calculation for BR estimation.

TABLE 8.2: Heart Rate and Breathing Rate Error Estimations for Cats at 20 cm, 30 cm, 40 cm, and 80 cm Distance by Using Different Phase Calculation Methods.

| Method | AVG Estimated HR (bpm) | AVG MAE BR (bpm) | AVG MEP BR (%) |
|---|---|---|---|
| Arctangent | 128.11 | 3.68 | 15.165 |
| DACM | 127.52 | 6.1 | 24.54 |
| EDACM | 121.44 | 2.26 | **9.26** |

### 8.2.4 Implementation 3 - BR Estimation

In the Table 8.3, different methods for BR estimation directly are compared: Peak Counting, FFT, and Rife. Here, both FFT and Rife methods show remarkably similar performances, with Rife slightly higher in MAE BR (2.34 bpm) and MEP BR (9.57%) compared to FFT's MAE BR (2.26 bpm) and MEP BR (9.26%). This indicates that both FFT and Rife are closely matched in accuracy for BR estimation, with a slight edge for FFT. Peak Counting, however, results in higher AVG MAE BR (5.26 bpm) and AVG MEP BR (21.29%), showcasing it as the least precise method among the three for BR estimation.

TABLE 8.3: Heart Rate, and Breathing Rate Error Estimations for Cats at Various Distances.

| Method | AVG Estimated HR (bpm) | AVG MAE BR (bpm) | AVG MEP BR (%) |
|---|---|---|---|
| Peak Counting | 122.1 | 5.26 | 21.29 |
| FFT | 121.44 | 2.26 | **9.26** |
| Rife | 121.44 | 2.34 | 9.57 |

## 8.3 Discussion

In this study, different methods were tried to measure cats' vital signs using the same radar system set up previously described. Measuring from different distances, like 65 cm, 40 cm, 30 cm, and 20 cm, showed that getting closer generally gave better readings for both heart and breathing rates. Trying to get a good heart rate measurement was especially tough.

Various reference sensors were tested, including the Polar H10 belt, the Polar Verity Sense, and the Contec08a-vet. Unfortunately, they did not give reliable readings. The Contec08a-vet seemed promising at first but using it was a challenge. It was hard to use it alongside the radar because someone had to be there to hold the sensor on the cat, which got in the way of the radar. Furthermore, the cats did not like the pressure the sensor put on their paws. It was a big challenge to get a heart rate reference, but breathing rates were still measurable, especially when the cats were sleeping.

For the radar data, different ways to work with the information were tested. For example, looking into out the best way to correct for DC offset did not make any difference, just like with human data. When it came to calculating phases, the EDACM method worked best for breathing rates, making it clear that this approach was more accurate than others.

Comparing methods for estimating breathing rates directly showed that FFT and Rife were close in accuracy, but FFT was slightly better. Peak Counting was not as accurate.

## 8.4    Research Question 3 Answered

Reflecting on the third research question, "How do these vital sign signal processing algorithms differ between human and animal monitoring?" the chapter reveals that the same signal processing algorithms, such as the EDACM for phase calculation and FFT for direct BR estimation, are essential in both contexts. However, adaptations to their parameters are necessary to account for the higher HR and BR in animals. The filter settings and threshold adjustments for peak counting are specifically tailored to cats, demonstrating the need for algorithmic flexibility to accommodate different physiological signatures. Notably, while FFT slightly outperformed Rife in BR estimation, its advantage emphasizes the importance of selecting and tuning methods based on the subject, whether human or animal. These findings are pivotal for advancing radar-based vital sign monitoring in a variety of living subjects.

# Chapter 9

# Activity Recognition Signal Processing

This chapter outlines essential signal processing steps for mmWave FMCW radar-based activity recognition. Beginning with Range-FFT, as detailed in Section 6.1.1, subsequent sections cover vital techniques such as time windowing, Doppler-FFT, and Micro-Doppler Spectrogram analysis. The chapter concludes with the integration of machine learning for activity recognition.

## 9.1   Time Windowing

By applying a window function, such as Hamming, Hanning, or STFT, spectral leakage can be decreased and spectral estimation improved. More information about STFT can be found in Section 6.1.1.

**Hanning Window:**   The Hanning window is defined by the formula:

$$w(n) = 0.5 - 0.5 \cos\left(\frac{2\pi n}{N-1}\right)$$

where $n$ is the sample index, and $N$ is the total number of samples in the window. It provides a good attenuation of side lobes compared to the Hamming window, making it particularly suitable for applications where accurate amplitude information is crucial.

**Hamming Window:**   The Hamming window is defined by the formula:

$$w(n) = 0.54 - 0.46 \cos\left(\frac{2\pi n}{N-1}\right)$$

where $n$ is the sample index, and $N$ is the total number of samples in the window. Similar to the Hanning window, the Hamming window is widely used in signal processing to reduce spectral leakage. It has a faster roll-off and a narrower main lobe compared to the Hanning window, but it comes at the expense of higher side lobes.

## 9.2   Doppler-FFT

If STFT is used, Doppler-FFT does not need to be applied, since STFT alreayd implies not only time windowing, but also FT applying to the time windows. But, if Hanning or

Hamming windowing is applied, Doppler-FFT should follow. The Doppler FFT is a key component in radar signal processing, specifically designed to analyze the frequency shifts induced by the motion of targets. If a time-domain signal $x(n)$ has been windowed with a Hanning window $w(n)$, for example, the Doppler FFT is applied to the resulting signal $x_w(n)$ to extract Doppler information. The formula for the Doppler FFT is as follows:

$$X_d(m, f) = \text{FFT}\{x_w(n)\}$$

where $X_d(m, f)$ represents the Doppler spectrum at time index $m$ and frequency index $f$. $\text{FFT}\{x_w(n)\}$ is the Fast Fourier Transform applied to the windowed signal.

The resulting $X_d(m, f)$ provides information about the Doppler shifts corresponding to the motion of targets. Each column in the Doppler spectrogram ($X_d$) corresponds to a specific time index ($m$), and each row corresponds to a frequency index ($f$). The amplitude or magnitude of $X_d(m, f)$ at a given time and frequency provides insights into the presence and motion characteristics of targets.

## 9.3  Micro-Doppler Spectrogram

The micro-Doppler spectrogram, derived from the Doppler shift caused by the motion of targets, encodes valuable information about the dynamics of moving objects. It extends the concept of the Doppler effect, which characterizes the change in frequency or wavelength of a wave in relation to an observer moving relative to the wave source, to capture the micro-motions of targets, such as limb movements in humans or animals.

### 9.3.1  Information Contained in Micro-Doppler Spectrograms

Micro-Doppler spectrograms present a time-frequency representation of these micro-motions, offering insights into:

- The nature of the movement (e.g., walking, running, falling) through the modulation patterns observed in the spectrogram.

- The speed and acceleration of different parts of the target, discernible through the frequency shifts.

- The structural characteristics of the target, such as limb length and gait cycle, inferred from the periodicity and intensity of the micro-Doppler signatures.

### 9.3.2  Accuracy and Limitations

The accuracy of micro-Doppler spectrograms in activity recognition largely depends on the radar system's resolution and the signal processing algorithms used. High-resolution radar systems can provide detailed micro-Doppler signatures, allowing for accurate activity classification. However, the presence of noise, interference from other moving objects, and the target's orientation relative to the radar can affect the clarity and interpretability of the micro-Doppler signatures.

Machine learning algorithms, particularly those capable of processing time-series data, such as CNNs and LSTMs, have shown promise in extracting relevant features from micro-Doppler spectrograms for activity recognition with high accuracy.

## 9.4 Machine Learning

This section introduces various classifiers commonly utilized in HAR studies mentioned in Section 2.2.1.

Support Vector Machines (SVM) are widely used for activity recognition due to their ability to handle complex decision boundaries. Additionally, SVMs with a decision-tree structure provide interpretability. Tools like LibSVM seem to be used and offer efficient implementation of SVM, where sequential minimal optimization (SMO) algorithm for kernelized SVMs are also implemented. SVM-Quadratic variants enhance classification accuracy through quadratic decision boundaries. Convolutional Neural Networks (CNN) are adept at capturing spatial dependencies in time series data. CNNs, often enhanced with activation functions like Leaky ReLU, prove effective for feature extraction in activity recognition tasks. Deep Neural Networks (DNN) offer a powerful framework for learning intricate patterns within data. In activity recognition, DNNs can automatically discover hierarchical representations, contributing to improved classification performance. K-Nearest Neighbors (KNN) is a straightforward yet effective algorithm, relying on proximity-based voting. While computationally intensive, KNN is advantageous for its simplicity and adaptability to various datasets. GoogleNet, also known as Inception, leverages intricate neural network architectures to enhance feature extraction. Its multi-path structure enables the model to capture diverse aspects of activity patterns, contributing to robust classification. Multilayer Perceptrons (MLP) form the basis of many deep learning models. In activity recognition, MLPs are employed for their capability to model complex relationships and non-linearities in the data. Bidirectional Long Short-Term Memory networks (Bi-LSTM), and their simpler counterpart, LSTM, excel at capturing temporal dependencies in sequential data. Bi-LSTM, in particular, considers both past and future context, making it well-suited for activity recognition tasks.

# Chapter 10

# Activity Recognition

## 10.1 Methodology

### 10.1.1 Devices Used

The data acquisition process for activity recognition employed the TI AWR1642BOOST radar sensor [1], in conjunction with the EVM DCA1000 [2], to capture raw radar signals. The setup's configuration parameters for the AWR1642BOOST, pivotal for the activity recognition task, are summarized in Table 10.1. This configuration was optimized for high-resolution data capture, crucial for distinguishing between different types of activities. The software facilitating data acquisition and initial processing is consistent with the setup described in Section 7, ensuring seamless integration and data consistency across different applications.

TABLE 10.1: Configuration Parameters of AWR1642BOOST for Activity Recognition.

| Parameter | Value |
| --- | --- |
| Start Frequency | 77 GHz |
| Frequency Slope | 88.883 MHz/$\mu s$ |
| ADC Start time | 4 $\mu s$ |
| ADC Samples | 256 |
| Sample Rate | 6250 ksps |
| Ramp End Time | 45 $\mu s$ |
| Chirp Count | 256 |
| Chirp Loop Count | 256 |
| Frame Count | 300-5000 |
| Frame Periodicity | 30 ms |
| RX Gain | 30 dB |
| TX Count | 2 |
| RX Count | 4 |

The configuration of the AWR1642BOOST radar sensor results in specific operational parameters critical for activity recognition. These parameters, derived from the configuration settings listed previously, dictate the radar's performance in terms of spatial resolution,

detection range, and velocity measurement capabilities.

### 10.1.2 Participant Information

Two indoor European Shorthair cats participated in the experiment, weighing 5.1 kg and 4.9 kg and aged 2.5 years and 1.7 years, respectively. Both are castrated males and do not have any known health issues.

### 10.1.3 Experiment Setup

The experiments were conducted in the natural home environment of the cats. Six distinct activities were recorded, with the specifics of each activity and its setup detailed in the subsequent sections. The Table 10.2 provides a summary of the recorded activities.

| Activity | Rec. per Cat | Duration (sec) | Total Rec. (Both Cats) | Total Time (sec, Both Cats) |
|---|---|---|---|---|
| Eating | 37 | 4 | 74 | 296 |
| Walking L to R | 37 | 4 | 74 | 296 |
| Walking Towards | 37 | 4 | 74 | 296 |
| Jumping | 37 | 4 | 74 | 296 |
| Walking w/ Human | 37 | 4 | 74 | 296 |
| Human Walking | 37 | 4 | 74 | 296 |

TABLE 10.2: Summary of Experiment Activities.

**Eating:** For the eating activity recording, the radar was positioned at an elevation of 3 cm above the floor. The antennas were situated approximately 8 cm from the bottom of the board, resulting in a total antenna elevation of 11 cm. The cat's food bowl was placed 50 cm away from the radar to ensure optimal data capture. A shallow bowl was used for the food to maximize the detection of the cat's mouth movements during eating. Additionally, the wall behind the cat was positioned approximately 2.2 m away from the setup. Figures 10.1 illustrate the setup for the eating activity, both schematically and in reality.



FIGURE 10.1: *Eating* Activity - Planned Setup.

**Walking from Left to Right:** For capturing the activity of a cat walking from left to right (from the radar's perspective), the radar was positioned approximately 1 meter parallel to the cat's walking path. The path covered by the cat extended about 2.5 meters. To achieve an optimal radar angle, the total elevation of the radar antennas was set to 25

cm, necessitating the placement of a 17 cm high box beneath the radar unit. Figure 10.2 illustrates this setup, with the depiction of multiple cat figures representing the trajectory of a single cat's movement across the observed path. Note that in the figure the cat is walking from right to left, but all the recordings were made when walking from left to right.
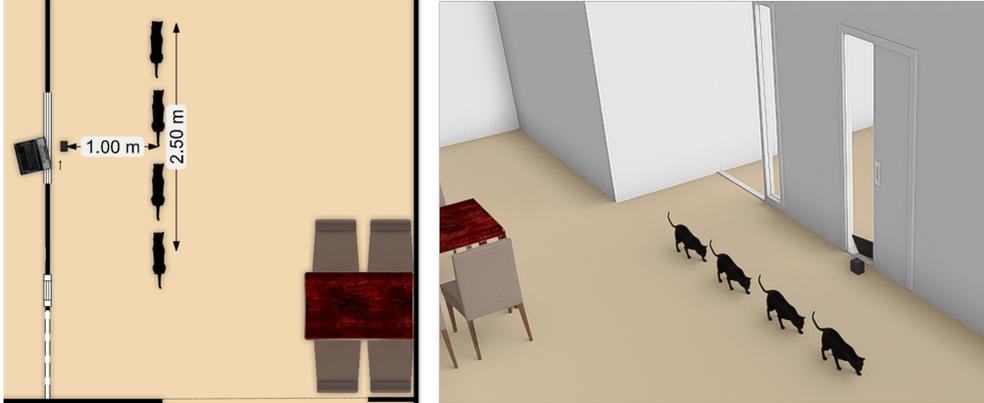


FIGURE 10.2: *Walking from the Side* Activity - Setup.

**Walking Towards:** The setup for walking towards activity, where the cat moves directly towards the radar, is depicted in Figures 10.3 and 10.4. The distance covered by the cat in this activity is approximately 2.5 meters. To ensure an optimal radar detection angle, the radar antennas were elevated to a total height of 25 cm above the ground, achieved by placing a 17 cm high box beneath the radar. This setup facilitates accurate data capture as the cat approaches the radar.
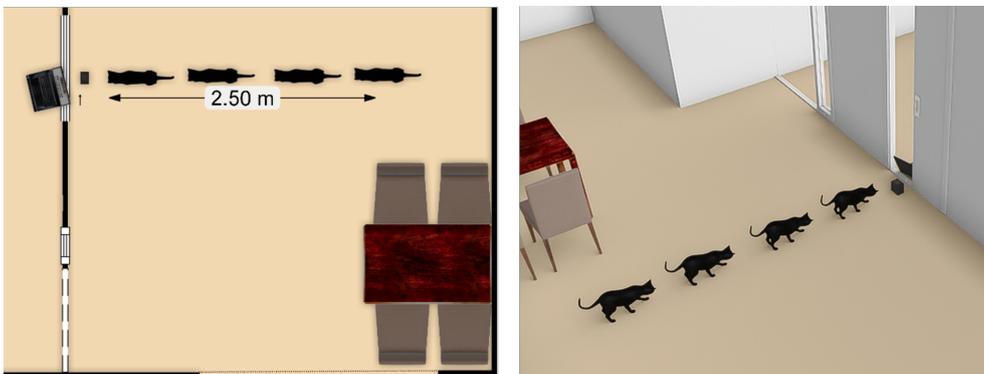


FIGURE 10.3: *Walking Towards* Activity - Planned Setup.
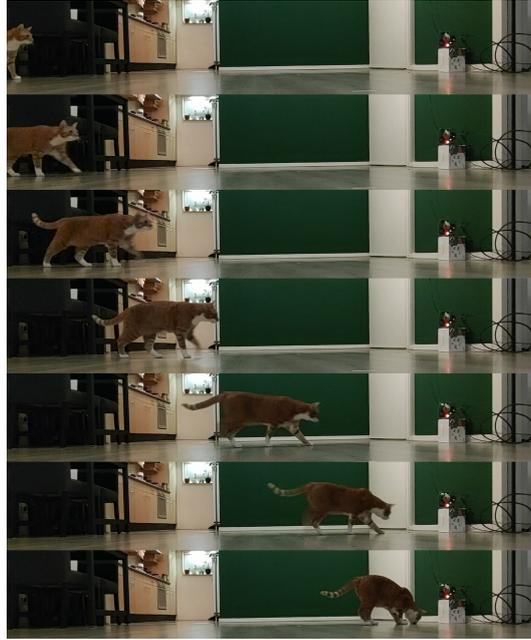
FIGURE 10.4: *Walking Towards* Activity - Real Setup.

**Jumping:** For the jumping activity, the setup was arranged with the cat performing jumps at a distance of approximately 1 meter from the radar, as depicted in Figure 10.5. To achieve the required radar detection angle, the total elevation of the radar antennas was set to 25 cm.



FIGURE 10.5: *Jumping* Activity - Real Setup.

**Walking with a Human:** This activity involved a human walking in the radar's view alongside the cat, both moving from left to right as previously shown in Figure 10.2. The objective was for the human to maintain a parallel distance of approximately 1 meter from the radar, with the cat walking at the same pace on the right side, closer to the radar. The arrangement aimed to capture the dynamics between the cat and the human during their simultaneous movement. The setup is depicted in Figure 10.6. To ensure an optimal radar detection angle, the radar antennas were elevated to a total height of 25 cm.

FIGURE 10.6: *Walking with a Human* Activity - Real Setup.

**Human Walking:** This activity involved a human walking in the radar's view alone (without a cat), moving from left to right as previously shown in Figure 10.2. The objective was for the human to maintain a parallel distance of approximately 1 meter from the radar, similarly as was done with a cat. Also, the pace was kept the same as if walking with a cat in the previously mentioned activity.

## 10.2    Data Processing

The block diagram of the signal processing steps performed for activity recognition is illustrated in Figure 10.7. The data is arranged in three dimensions: one dimension represents the number of receive (Rx) channels, the second dimension corresponds to time, encapsulating both chirps and frames, and the third dimension represents the ADC samples. Initially, the mean value across the Rx channels is calculated, effectively reducing the data along one dimension. This preprocessing step aids in noise minimization and signal enhancement. Subsequently, a range-FFT is applied to the ADC samples within a frame, transforming the signal to the frequency domain. A summation across the range bins is then performed, effectively collapsing another dimension and further reducing noise. Following this, a Hanning window is applied to each chirp to mitigate spectral leakage, complemented by zero padding to increase the FFT resolution. A Doppler-FFT is next, revealing Doppler frequencies associated with movement. The spectrogram is generated by converting these Doppler frequencies to decibels, providing a visual representation of frequency over time. As a final step, residual noise is filtered out through the calculation and subtraction of the mean values from the Doppler shifts, enhancing the clarity of the spectrogram for activity recognition.
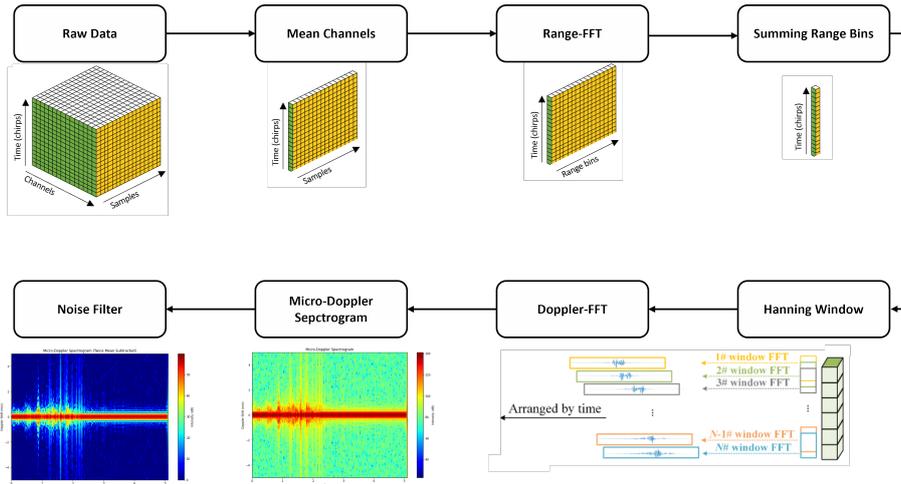
FIGURE 10.7: Signal Processing Block Diagram for Activity Recognition.

### 10.2.1 Micro-Doppler Spectrograms

After obtaining the spectrograms, they are cut to be 4 seconds of duration and saved. Example spectrograms of the recorded activities can be seen in Figure B.1 to Figure B.5 in Appendix B. Afterwards, these 4 second long spectograms are saved as CSV file, naming it appropriately to indicate the activity and the participant. Each corresponding activity is saved in a folder named accordingly.

### 10.2.2 Classifier Structure and Parameters

**CNN + LSTM Classifier**   This classifier employs a hybrid neural network architecture that integrates time-distributed CNN layers with a Bi-Directional LSTM for robust activity recognition from spectrogram data. The network's backbone consists of three sets of double-layered convolutional blocks, each time-distributed to process individual time slices and followed by max pooling to distill features. This setup captures the intricate spatial patterns across time steps. Subsequent to the CNN layers, a Bi-Directional LSTM harnesses both past and future context for temporal feature extraction. The model concludes with a softmax output layer, adapted for multi-class classification. Trained for 30 epochs with an Adam optimizer and categorical crossentropy loss, the model's learning process is fine-tuned via checkpoints based on validation performance, ensuring a balance between accuracy and generalization.

**Bi-directional LSTM Classifier**   The LSTM classifier architecture utilizes a bidirectional approach to sequence processing, allowing the model to learn from both past and future contexts simultaneously. By duplicating the LSTM layer, with one layer processing from past to future and the other from future to past, the model can capture dependencies throughout the sequence more effectively. The network consists of a singular Bi-Directional LSTM layer, which is then followed by two fully connected layers. A final softmax output layer is used for multi-class classification.

In the implementation, the classifier's training begins with preprocessing, including one-hot encoding of the target labels. The dataset is then split into a training set and a testing set, with a 75-25% split ratio, and stratification is applied to preserve the class distribution. The model is trained for 30 epochs with a batch size of 20, using the Adam optimizer and categorical crossentropy loss function. Training progress is monitored and

optimized using model checkpoints based on validation loss, ensuring the retention of the most effective version of the model. The model's classification ability is assessed via a confusion matrix, which visually demonstrates the classifier's performance across the different activity classes.

**SVM Classifier**   The SVM classifier uses a flattened feature vector for each data instance and reduces dimensionality through Principal Component Analysis (PCA) to capture the most informative aspects of the data while minimizing computational complexity. Employing an RBF kernel, the SVM operates within a transformed feature space to find the optimal hyperplane that separates classes. Hyperparameters are fine-tuned via GridSearchCV, ensuring that the model is well-adjusted to the dataset's characteristics. The PCA process is pivotal, reducing the features from 10,000 to a more manageable 330 principal components, thus retaining the most critical information for classification. Training and evaluation of the SVM are conducted on these condensed feature sets, and the classifier's accuracy is substantiated through a confusion matrix and hinge loss metrics, providing insight into the model's predictive power and precision.

**MLP Classifier**   The MLP classifier is architected to leverage a deep network of fully connected layers for classification tasks. After input data is flattened to form a 1D feature vector, it progresses through multiple dense layers interlaid with dropout and batch normalization to prevent overfitting and ensure efficient training. Each dense layer employs ReLU activation to introduce non-linearity, enabling the model to learn complex patterns in the data. The architecture culminates in a softmax output layer, allowing for multi-class categorization. Trained on a stratified split dataset for 30 epochs, the MLP's configuration is optimized using an Adam optimizer with a learning rate of 0.001. Model performance is validated using accuracy metrics and visualized through a confusion matrix, providing an intuitive understanding of its classification prowess.

## 10.3   Results

The classifiers utilized in this research were adapted from the work by Singh, Akash Deep, et al. [94]. This work has provided a comprehensive suite including datasets, preprocessing tools, and classifiers designed for activity recognition. The classifier confusion matrices for classifying activities of both cats can be found in Appendix C Figures C.1 to C.4.

### 10.3.1   CNN + LSTM Classifier

The Time-distributed CNN + Bi-directional LSTM Classifier yielded a high training accuracy of 76.50% when applied to both cats' data. However, the test accuracy was significantly lower at 61.26%. The substantial gap between train and test accuracies, coupled with a value loss of 1.015, indicates that the model may be overfitting to the training data, capturing noise rather than the underlying pattern.

TABLE 10.3: Time-distributed CNN + Bi-directional LSTM Classifier Accuracy.

| Scenario | Train Accuracy | Value Loss | Test Accuracy |
|---|---|---|---|
| Both Cats | 76.50 | 1.015 | 61.26 |
| First Cat | 84.24 | 1.213 | 48.21 |
| Second Cat | 77.70 | 1.136 | 53.57 |

### 10.3.2 Bi-directional LSTM Classifier

The Bi-directional LSTM Classifier also exhibited a discrepancy between training and testing performance, with a training accuracy of 73.19% and a test accuracy of 51.35%. This performance differential suggests difficulties in the model's ability to generalize, which could be due to the LSTM layers memorizing specific sequences.

TABLE 10.4: Bi-directional LSTM Classifier Accuracy.

| Scenario | Train Accuracy | Value Loss | Test Accuracy |
|---|---|---|---|
| Both Cats | 73.19 | 1.167 | 51.35 |
| First Cat | 87.88 | 1.316 | 44.64 |
| Second Cat | 86.75 | 1.220 | 55.36 |

### 10.3.3 SVM Classifier

Interestingly, the SVM Classifier showed consistent performance between training and testing with an accuracy of 74.77%. The lower hinge loss of 0.723 indicates that the SVM's linear decision boundary is effective in this classification context, possibly due to the SVM's maximization of the margin which provides robustness to variations within the data.

TABLE 10.5: SVM Classifier Accuracy.

| Scenario | Train Accuracy | Hinge Loss | Test Accuracy |
|---|---|---|---|
| Both Cats | 74.77 | 0.723 | **74.77** |
| First Cat | 75.00 | 0.842 | 67.86 |
| Second Cat | 73.21 | 0.997 | 67.86 |

### 10.3.4 MLP Classifier

The MLP Classifier demonstrated an atypical result with a training accuracy of 55.00% and a test accuracy of 70.27%. This inversion where test accuracy exceeds training accuracy could suggest that the model's simplicity results in underfitting and that the test data may contain less complex patterns or be inadvertently aligned with the decision boundaries formed.

TABLE 10.6: MLP Classifier Accuracy.

| Scenario | Train Accuracy | Value Loss | Test Accuracy |
|---|---|---|---|
| Both Cats | 55.00 | 1.031 | 70.27 |
| First Cat | 59.39 | 1.130 | 53.57 |
| Second Cat | 43.37 | 1.176 | 42.86 |

## 10.4 Discussion

A comparison of classifier performances highlights the impact of model architecture and data representation on the ability to generalize. The CNN + LSTM and LSTM classifiers showed significant overfitting, evident from their high training accuracies and lower

test scores. This suggests a potential overparameterization, where the models learn the idiosyncrasies of the training data rather than the general characteristics of the activities.

In contrast, the SVM's consistent training and test accuracies indicate a strong ability to generalize, which may be attributed to the SVM's inherent capacity to find a hyperplane that maximizes the margin between classes in a high-dimensional space. The lower hinge loss further corroborates the SVM's robust classification capabilities.

The MLP's unexpected higher test accuracy suggests that while the network might be too simple to capture the complexities in the training data (underfitting), it might be suitably aligned with the test data. This raises questions about the diversity and complexity of the test data, suggesting a further need for dataset examination.

When comparing the performance of different classifiers, it's clear that the type of model used and how the data is shown to the model really matter. Some activities of the cats were not acceptable for micro-Doppler spectrograms, so they had to be left out. This made the data set uneven because initially, the goal was to have 27 activities for each cat, but because some activities were not as clear, more recordings were needed. Hence, later on 37 activities per cat were recorded to account for the unclear spectrograms obtained earlier, and to obtain more data overall.

It was also challenging to get the cats to do the activities the same way every recording time. For example, sometimes a cat would run towards the radar, and other times it would walk. This inconsistency was a problem, especially for activities like walking towards the radar, which resulted in being the hardest to classify correctly. The confusion matrix in the appendix shows this too.

Another challenge was that many activities looked similar when looked at through spectrogram, such as walking by and eating, or a human walking by alone versus with a cat. This made it difficult to tell the activities apart. Trying to record more distinct activities like licking and drinking was considered, but it was considered to be too difficult at the time to manage.

Overall, the results underline the need for careful consideration of model complexity and generalization. They also suggest that different models may require different strategies for regularization and that the complexity of the test data should always be scrutinized.

## 10.5   Research Question 4 Answered

Reflecting on the fourth research question, "How can FMCW radar technology be applied to recognize and classify different animal activities, and what are the implications of these capabilities for understanding animal behavior and health?" the findings elucidate that FMCW radar technology, through micro-Doppler signatures, effectively distinguishes between various animal activities. The application of sophisticated signal processing techniques and machine learning classifiers, particularly SVM, enables the classification of these activities with notable accuracy (74.77%). This capacity to monitor and recognize behavior patterns non-invasively holds significant potential for advancing our understanding of animal health and wellbeing. It can lead to early detection of anomalies in behavior that may indicate health issues, providing a powerful tool for veterinary care and research into animal behavior. Notably, the classifier was also able to distinguish between the human walking, pet waling, and human walking with a cat, which is an interesting finding of human and pet motioning as one.

# Chapter 11

# Final Conclusions and Future Work

## 11.1 Answering the Main Research Question

This thesis set out to explore the potential of mmWave FMCW radar technology for non-invasive health monitoring in humans and pets, addressing the overarching question: "What is the potential of mmWave FMCW radar technology in enhancing non-invasive health monitoring for humans and pets?" The findings underscore the technology's profound capacity to accurately detect vital signs and classify behaviors without direct contact. Specifically, for human health monitoring, adaptations of the Rife Algorithm and EDACM emerged as pivotal in capturing heart and breathing rates accurately. When applied to pets, the technology demonstrated its versatility by adjusting to higher vital sign frequencies and effectively classifying various animal activities through micro-Doppler signatures. These capabilities not only open the way for new approaches to health monitoring but also offer new insights into the daily lives and well-being of both humans and animals.

## 11.2 Suggestions for Future Work

The potential applications and improvements of this technology are vast, pointing to several exciting avenues for future research:

- **Enhancing Signal Processing Techniques:** Further research should focus on optimizing the algorithms used for signal processing to improve the technology's sensitivity and specificity across different species and conditions. Developing more sophisticated algorithms could lead to earlier detection of health anomalies.

- **Broadening Activity Recognition:** Expanding the repertoire of recognizable activities, especially for pets, could significantly enhance our understanding of animal behavior and health. This involves not only capturing more activities but also refining the classification algorithms to distinguish between similar behaviors more effectively.

- **Developing Real-time Monitoring Solutions:** There's a critical need for systems capable of processing data in real-time to provide immediate feedback or alerts. This could be particularly beneficial in critical care situations, offering a lifeline through timely intervention.

# Bibliography

[1] Awr1642boost. Accessed on 01-02-2024. URL: https://www.ti.com/tool/AWR1642BOOST.

[2] Dca1000evm. Accessed on 01-02-2024. URL: https://www.ti.com/tool/DCA1000EVM.

[3] FitBit Smartwatch. https://www.fitbit.com/. Accessed: 21-03-2023.

[4] PetPace - Monitor Your Pets Health. https://petpace.com/. Accessed: 21-03-2023.

[5] Polar h10 chest strip - heart rate sensor. Accessed on 21-03-2023. URL: https://www.polar.com/us-en/sensors/h10-heart-rate-sensor/.

[6] VitalTracer - SMART WEARABLE DEVICES THAT MEASURE ALL VITAL SIGNS CONTINUOUSLY. https://vitaltracer.com/. Accessed: 21-03-2023.

[7] Jonathan A Abbott. Heart rate and heart rate variability of healthy cats in home and hospital environments. *Journal of feline medicine and surgery*, 7(3):195–202, 2005.

[8] Hadi Alidoustaghdam, Min Chen, Ben Willetts, Kai Mao, André Kokkeler, and Yang Miao. Enhancing vital sign estimation performance of fmcw mimo radar by prior human shape recognition. *arXiv preprint arXiv:2303.09400*, 2023.

[9] Mostafa Alizadeh, George Shaker, João Carlos Martins De Almeida, Plinio Pelegrini Morita, and Safeddin Safavi-Naeini. Remote monitoring of human vital signs using mm-wave fmcw radar. *IEEE Access*, 7:54958–54968, 2019.

[10] Christoph Hoog Antink, Simon Lyra, Michael Paul, Xinchi Yu, and Steffen Leonhardt. A broader look: Camera-based vital sign estimation across the spectrum. *Yearbook of medical informatics*, 28(01):102–114, 2019.

[11] Serdal Ayhan, Steffen Scherr, Akanksha Bhutani, Benjamin Fischbach, Mario Pauli, and Thomas Zwick. Impact of frequency ramp nonlinearity, phase noise, and snr on fmcw radar accuracy. *IEEE Transactions on Microwave Theory and Techniques*, 64(10):3290–3301, 2016.

[12] Thomas Bien and Barbara Bien. Breathing variability: A review of the theoretical framework and clinical implications. *Journal of Respiratory Medicine*, 105(12):1753–1760, 2011.

[13] Gies Broeder. Human activity recognition using a mmwave radar. B.S. thesis, University of Twente, 2022.

[14] David Brown and Harpreet Singh. Radar technology in healthcare: A review. *Journal of Radar and Healthcare*, 2(4):234–245, 2021.

[15] Nicholas P. Burnett, Rui Seabra, Maurizio de Pirro, David S. Wethey, Sarah A. Woodin, Brian Helmuth, Mackenzie L. Zippay, Gianluca Sarà, Cristián Monaco, and Fernando P. Lima. An improved noninvasive method for measuring heartbeat of intertidal animals. *Limnology and Oceanography: Methods*, 11(2):91–100, 2013. URL: https://aslopubs.onlinelibrary.wiley.com/doi/abs/10.4319/lom.2013.11.91, arXiv:https://aslopubs.onlinelibrary.wiley.com/doi/pdf/10.4319/lom.2013.11.91, doi:10.4319/lom.2013.11.91.

[16] Sergio Giuseppe Cananzi, Luke A White, Mansoureh Barzegar, Christen J Boyer, Oleg Y Chernyshev, J Winny Yun, RE Kelley, Isaac Almendros, Alireza Minagar, Ramon Farré, et al. Obstructive sleep apnea intensifies stroke severity following middle cerebral artery occlusion. *Sleep Medicine*, 67:278–285, 2020.

[17] Lin Cao, Ran Wei, Zongmin Zhao, Dongfeng Wang, and Chong Fu. A novel frequency tracking algorithm for non-contact vital sign monitoring. *IEEE Sensors Journal*, 2023.

[18] P.H. Charlton, T. Bonnici, L. Tarassenko, D.A. Clifton, R. Beale, and P.J. Watkinson. Assessment of heart and respiratory rates using dual impedance pneumography in a wearable device. *Medical & Biological Engineering & Computing*, 55(5):907–920, 2017.

[19] Zekun Chen, Yunxue Liu, and Zhuoran Cai. Noncontact heart rate detection method based on kalman filter. In *2022 Global Reliability and Prognostics and Health Management (PHM-Yantai)*, pages 1–5. IEEE, 2022.

[20] Zekun Chen, Yunxue Liu, Chenhong Sui, Min Zhou, and Yuqing Song. A novel scheme for suppression of human motion effects in non-contact heart rate detection. *IEEE Access*, 2023.

[21] Sergei Churkin and Lesya Anishchenko. Millimeter-wave radar for vital signs monitoring. In *2015 IEEE International Conference on Microwaves, Communications, Antennas and Electronic Systems (COMCAS)*, pages 1–4. IEEE, 2015.

[22] Charles Cook. *Radar signals: An introduction to theory and application*. Elsevier, 2012.

[23] Lei Ding, Murtaza Ali, Sujeet Patole, and Anand Dabak. Vibration parameter estimation using fmcw radar. In *2016 IEEE International Conference on Acoustics, Speech and Signal Processing (ICASSP)*, pages 2224–2228. IEEE, 2016.

[24] Amy Diane Droitcour. *Non-contact measurement of heart and respiration rates with a single-chip microwave doppler radar*. Stanford University, 2006.

[25] Task Force of the European Society of Cardiology the North American Society of Pacing Electrophysiology. Heart rate variability: standards of measurement, physiological interpretation, and clinical use. *Circulation*, 93(5):1043–1065, 1996.

[26] Julien Fatisson, Victoria Oswald, and François Lalonde. Influence of exercise on heart rate variability: An updated meta-analysis. *Physical Therapy and Rehabilitation*, 3(1), 2016.

[27] James Foulkes, Peter Tucker, Mariflor Caronan, Rebecca Curtis, Leslie G Parker, Chris Farnell, Brett Sparkman, Guoqing Zhou, Scott C Smith, and Jingxian Wu. Livestock management system. In *Proceedings of the International Conference on Embedded Systems, Cyber-physical Systems, and Applications (ESCS)*, page 1. The Steering Committee of The World Congress in Computer Science, Computer . . . , 2013.

[28] Thomas Gänzle, Clemens Klöck, and Karsten Heuschkel. Real-time vital sign detection using a 77 ghz fmcw radar. In *2022 IEEE-EMBS Conference on Biomedical Engineering and Sciences (IECBES)*, pages 148–153. IEEE, 2022.

[29] R. Gilgen-Ammann, V. Schweinler, and T. Wyss. Accuracy and reliability of polar h10 compared to an electrocardiogram device. *International Journal of Sports Medicine*, 40(6):363–372, 2019.

[30] Marco Giordano, Gamze Islamoglu, Viviane Potocnik, Christian Vogt, and Michele Magno. Survey, analysis and comparison of radar technologies for embedded vital sign monitoring. In *2022 44th Annual International Conference of the IEEE Engineering in Medicine & Biology Society (EMBC)*, pages 854–860. IEEE, 2022.

[31] Emma K Grigg, Yu Ueda, Ashley L Walker, Lynette A Hart, Samany Simas, and Joshua A Stern. Comparative assessment of heart rate variability obtained via ambulatory ecg and polar heart rate monitors in healthy cats: a pilot study. *Frontiers in Veterinary Science*, 8:741583, 2021.

[32] Changzhan Gu, Guochao Wang, Yiran Li, Takao Inoue, and Changzhi Li. A hybrid radar-camera sensing system with phase compensation for random body movement cancellation in doppler vital sign detection. *IEEE transactions on microwave theory and techniques*, 61(12):4678–4688, 2013.

[33] Changzhan Gu, Jian Wang, and Jaime Lien. Deep neural network based body movement cancellation for doppler radar vital sign detection. In *2019 IEEE MTT-S International Wireless Symposium (IWS)*, pages 1–3. IEEE, 2019.

[34] Babak Hassibi and Bertrand M Hochwald. How much training is needed in multiple-antenna wireless links? *IEEE Transactions on Information Theory*, 49(4):951–963, 2003.

[35] Mi He, Yongjian Nian, and Yushun Gong. Novel signal processing method for vital sign monitoring using fmcw radar. *Biomedical Signal Processing and Control*, 33:335–345, 2017.

[36] Barry Hill and Sarah H Annesley. Monitoring respiratory rate in adults. *British journal of nursing*, 29(1):12–16, 2020.

[37] Hans-Günter Hirsch, Jan Stähler, Manfred Hägelen, and Reinhard Kulke. Analyzing the classification capability of micro-doppler spectra. In *2020 IEEE Radar Conference (RadarConf20)*, pages 1–6. IEEE, 2020.

[38] J Holzworth, P Theran, JL Carpenter, NK Harpster, and RJ Todoroff. Hyperthyroidism in the cat: ten cases. *Journal of the American Veterinary Medical Association*, 176(4):345–353, 1980.

[39] Wei Hu, Zhangyan Zhao, Yunfeng Wang, Haiying Zhang, and Fujiang Lin. Noncontact accurate measurement of cardiopulmonary activity using a compact quadrature doppler radar sensor. *IEEE Transactions on Biomedical Engineering*, 61(3):725–735, 2013.

[40] Qianlan Huang, Dawei Lu, Jiemin Hu, Hongqi Fan, Meirong Liang, and Jun Zhang. Simultaneous location and parameter estimation of human vital sign with mimo-fmcw radar. In *2019 IEEE International Conference on Signal, Information and Data Processing (ICSIDP)*, pages 1–4. IEEE, 2019.

[41] Tien-Yu Huang, Linda F Hayward, and Jenshan Lin. Noninvasive measurement and analysis of laboratory rat's cardiorespiratory movement. *IEEE Transactions on Microwave Theory and Techniques*, 65(2):574–581, 2016.

[42] Texas Instruments. Awr1642 evaluation module (awr1642boost) single-chip mmwave sensing solution, apr. 2018.

[43] Texas Instruments. Mmwave radar device adc raw data capture, application report, december 2017–revised october 2018.

[44] Prabhu Janakaraj, Kalvik Jakkala, Arupjyoti Bhuyan, Zhi Sun, Pu Wang, and Minwoo Lee. Star: simultaneous tracking and recognition through millimeter waves and deep learning. In *2019 12th IFIP Wireless and Mobile Networking Conference (WMNC)*, pages 211–218. IEEE, 2019.

[45] Shanling Ji, Haiying Wen, Jiankang Wu, Zhisheng Zhang, and Kunkun Zhao. Systematic heartbeat monitoring using a fmcw mm-wave radar. In *2021 IEEE International Conference on Consumer Electronics and Computer Engineering (ICCECE)*, pages 714–718. IEEE, 2021.

[46] Wen Jiang, Yihui Ren, Ying Liu, Ziao Wang, and Xinghua Wang. Recognition of dynamic hand gesture based on mm-wave fmcw radar micro-doppler signatures. In *ICASSP 2021-2021 IEEE International Conference on Acoustics, Speech and Signal Processing (ICASSP)*, pages 4905–4909. IEEE, 2021.

[47] Michael Jones and Sanjay Patel. Non-wearable sensors for health monitoring. *Innovations in Healthcare Technology*, 6(3):200–210, 2019.

[48] Maria Jorquera-Chavez, Sigfredo Fuentes, Frank R Dunshea, Robyn D Warner, Tomas Poblete, and Ellen C Jongman. Modelling and validation of computer vision techniques to assess heart rate, eye temperature, ear-base temperature and respiration rate in cattle. *Animals*, 9(12):1089, 2019.

[49] Steven Kesten, M Reza Maleki-Yazdi, Bruce R Sanders, Janet A Wells, Susan L McKillop, Kenneth R Chapman, and Anthony S Rebuck. Respiratory rate during acute asthma. *Chest*, 97(1):58–62, 1990.

[50] Youngwook Kim and Hao Ling. Human activity classification based on micro-doppler signatures using a support vector machine. *IEEE transactions on geoscience and remote sensing*, 47(5):1328–1337, 2009.

[51] Jun Lai, Jingyun Lu, Changzhan Gu, and Jun-Fa Mao. Non-contact vital sign monitoring of cat using continuous-wave doppler radar. In *2022 International Conference on Microwave and Millimeter Wave Technology (ICMMT)*, pages 1–3. IEEE, 2022.

[52] Alice Lee and Young Kim. Cardiovascular monitoring: From wearables to non-contact sensing. *Advanced Health Monitoring Systems*, 5(1):45–59, 2018.

[53] Jee-Hoon Lee and Seong-Ook Park. A 14 ghz non-contact radar system for long range heart rate detection. In *2013 Proceedings of the International Symposium on Antennas & Propagation*, volume 1, pages 204–206. IEEE, 2013.

[54] Changzhi Li and Jenshan Lin. Random body movement cancellation in doppler radar vital sign detection. *IEEE Transactions on Microwave Theory and Techniques*, 56(12):3143–3152, 2008.

[55] Chen Li and Peng Zhang. Radar sensing for remote health monitoring. *Sensor Review*, 36(4):429–437, 2016.

[56] Haobo Li, Aman Shrestha, Hadi Heidari, Julien Le Kernec, and Francesco Fioranelli. Bi-lstm network for multimodal continuous human activity recognition and fall detection. *IEEE Sensors Journal*, 20(3):1191–1201, 2019.

[57] Kang Liu, Chenxu Ding, and Yuanhui Zhang. A coarse-to-fine robust estimation of fmcw radar signal for vital sign detection. In *2020 IEEE Radar Conference (Radar-Conf20)*, pages 1–6. IEEE, 2020.

[58] Ingrid Ljungvall, Mark Rishniw, Francesco Porciello, Jens Häggström, and Dan Ohad. Sleeping and resting respiratory rates in healthy adult cats and cats with subclinical heart disease. *Journal of Feline Medicine and Surgery*, 16(4):281–290, 2014.

[59] Craig Lockwood, Tiffany Conroy-Hiller, and Tamara Page. Vital signs. *JBI reports*, 2(6):207–230, 2004.

[60] Fei Luo. *Human activity classification using micro-Doppler signatures and ranging techniques*. PhD thesis, Queen Mary University of London, 2020.

[61] Qinyi Lv, Dexin Ye, Shan Qiao, Yannick Salamin, Jiangtao Huangfu, Changzhi Li, and Lixin Ran. High dynamic-range motion imaging based on linearized doppler radar sensor. *IEEE Transactions on Microwave Theory and Techniques*, 62(9):1837–1846, 2014.

[62] Qinyi Lv, Dexin Ye, Shan Qiao, Yannick Salamin, Jiangtao Huangfu, Changzhi Li, and Lixin Ran. High dynamic-range motion imaging based on linearized doppler radar sensor. *IEEE Transactions on Microwave Theory and Techniques*, 62(9):1837–1846, 2014. doi:10.1109/TMTT.2014.2342663.

[63] Wenjie Lv, Wangdong He, Xipeng Lin, and Jungang Miao. Non-contact monitoring of human vital signs using fmcw millimeter wave radar in the 120 ghz band. *Sensors*, 21(8):2732, 2021.

[64] Yangyang Ma, Pengfei Wang, Huijun Xue, Fulai Liang, Fugui Qi, Hao Lv, Xiao Yu, Jianqi Wang, and Yang Zhang. Non-contact vital states identification of trapped living bodies using ultra-wideband bio-radar. *IEEE Access*, 9:6550–6559, 2020.

[65] Daniel McDuff. Camera measurement of physiological vital signs. *ACM Computing Surveys*, 55(9):1–40, 2023.

[66] W. Q. Mok, W. Wang, and S. Y. Liaw. Vital signs monitoring to detect patient deterioration: An integrative literature review. *International journal of nursing practice*, 21:91–98, 2015.

[67] Richard W Nelson and C Guillermo Couto. *Small animal internal medicine-E-book*. Elsevier Health Sciences, 2019.

[68] Steven Nguyen, Edward Vasquez, Oren Ofer, and PP Diniz. Quality and accuracy of the smartphone ecg in cats, 2016.

[69] Ameen Bin Obadi, Ping Jack Soh, Omar Aldayel, Muataz Hameed Al-Doori, Marco Mercuri, and Dominique Schreurs. A survey on vital signs detection using radar techniques and processing with fpga implementation. *IEEE Circuits and Systems Magazine*, 21(1):41–74, 2021.

[70] Kellen Oleksak. Vital sign detection using millimeter wave radars. 2020.

[71] Cristian A Ospina-De la Cruz, Humberto Pérez-Espinosa, Mariel Urbina-Escalante, Verónica Reyes-Meza, and Jorge Ríos-Martínez. Automatic assessment of canine trainability using heart rate responses to positive and negative emotional stimuli. In *Mexican International Conference on Artificial Intelligence*, pages 142–156. Springer, 2023.

[72] Min Park and Jong Lee. Advancements in radar technology for healthcare applications. *International Journal of Bio-Engineering and Technology*, 11(2):21–35, 2017.

[73] Polar Research and Technology. Polar h10 heart rate sensor system (white paper). https://www.polar.com/sites/default/files/static/science/white-papers/polar-h10-heart-rate-sensor-white-paper.pdf. (Accessed on 02/27/2024).

[74] A Raalte. Animal activity recognition using a fmcw millimeter wave radar. B.S. thesis, University of Twente, 2021.

[75] Md Atikur Rahman, Md Shahin Ali, and Shekh Md Mahmudul Islam. Non-contact vital signs monitoring in broiler chickens. 2023.

[76] Jesse M. Raiten, Ronald Eichel, and Daniel J. Raiten. Measurement of respiratory rate in adults: A review of available methods. *Journal of Clinical Monitoring and Computing*, 30(5):675–688, 2016.

[77] Theodore S Rappaport, Yunchou Xing, George R MacCartney, Andreas F Molisch, Evangelos Mellios, and Jianhua Zhang. Overview of millimeter wave communications for fifth-generation (5g) wireless networks—with a focus on propagation models. *IEEE Transactions on antennas and propagation*, 65(12):6213–6230, 2017.

[78] Lingyun Ren, Lingqin Kong, Farnaz Foroughian, Haofei Wang, Paul Theilmann, and Aly E Fathy. Comparison study of noncontact vital signs detection using a doppler stepped-frequency continuous-wave radar and camera-based imaging photoplethysmography. *IEEE Transactions on Microwave Theory and Techniques*, 65(9):3519–3529, 2017.

[79] Lingyun Ren, Haofei Wang, Krishna Naishadham, Quanhua Liu, and Aly E Fathy. Non-invasive detection of cardiac and respiratory rates from stepped frequency continuous wave radar measurements using the state space method. In *2015 IEEE MTT-S International Microwave Symposium*, pages 1–4. IEEE, 2015.

[80] Mark A. Richards, James A. Scheer, and William A. Holm. *Principles of Modern Radar: Basic Principles*. SciTech Publishing, 2nd edition, 2014.

[81] Mark A Richards, Jim Scheer, William A Holm, and William L Melvin. Principles of modern radar. 2010.

[82] Ehsan Sadeghi, Claudie Kappers, Alessandro Chiumento, Marjolein Derks, and Paul Havinga. Improving piglets health and well-being: A review of piglets health indicators and related sensing technologies. *Smart Agricultural Technology*, page 100246, 2023.

[83] Ehsan Sadeghi, Claudie Kappers, Alessandro Chiumento, Marjolein Derks, and Paul Havinga. Improving piglets health and well-being: A review of piglets health indicators and related sensing technologies. *Smart Agricultural Technology*, page 100246, 2023.

[84] Takuya Sakamoto, Ryohei Imasaka, Hirofumi Taki, Toru Sato, Mototaka Yoshioka, Kenichi Inoue, Takeshi Fukuda, and Hiroyuki Sakai. Feature-based correlation and topological similarity for interbeat interval estimation using ultrawideband radar. *IEEE Transactions on Biomedical Engineering*, 63(4):747–757, 2015.

[85] Frank Schadt, Friedemann Mohr, and Markus Holzer. Application of kalman filters as a tool for phase and frequency demodulation of iq signals. In *2008 IEEE Region 8 International Conference on Computational Technologies in Electrical and Electronics Engineering*, pages 421–424. IEEE, 2008.

[86] S. Schellenberger, K. Shi, T. Steigleder, A. Malessa, F. Michler, L. Hameyer, N. Neumann, F. Lurz, R. Weigel, C. Ostgathe, et al. A dataset of clinically recorded radar vital signs with synchronised reference sensor signals. *Scientific Data*, 7(1):291, 2020.

[87] B.J.A. Schijvenaars, R.A.P. Vanwersch, and H. Van Keulen. A comprehensive review of electrocardiogram-based analysis of heart rate variability. *International Journal of Cardiology*, 203:702–709, 2016.

[88] Fred Shaffer and J. P. Ginsberg. An overview of heart rate variability metrics and norms. *Frontiers in Public Health*, 5:258, 2017.

[89] Ghufran Shafiq and Kalyana C Veluvolu. Surface chest motion decomposition for cardiovascular monitoring. *Scientific reports*, 4(1):5093, 2014.

[90] Syed Aziz Shah and Francesco Fioranelli. Human activity recognition: Preliminary results for dataset portability using fmcw radar. In *2019 international radar conference (RADAR)*, pages 1–4. IEEE, 2019.

[91] Victor G Sharov, Anastassia Goussev, Michael Lesch, Sidney Goldstein, and Hani N Sabbah. Abnormal mitochondrial function in myocardium of dogs with chronic heart failure. *Journal of molecular and cellular cardiology*, 30(9):1757–1762, 1998.

[92] Arash Shokouhmand, Samuel Eckstrom, Behnood Gholami, and Negar Tavassolian. Camera-augmented non-contact vital sign monitoring in real time. *IEEE Sensors Journal*, 22(12):11965–11978, 2022.

[93] Aman Shrestha. *Radar based discrete and continuous activity recognition for assisted living*. PhD thesis, University of Glasgow, 2021.

[94] Akash Deep Singh, Sandeep Singh Sandha, Luis Garcia, and Mani Srivastava. Radhar: Human activity recognition from point clouds generated through a millimeter-wave radar. In *Proceedings of the 3rd ACM Workshop on Millimeter-wave Networks and Sensing Systems*, pages 51–56. ACM, 2019.

[95] John Smith and Jane Doe. The importance of monitoring vital signs. *Journal of Medical Innovation*, 4(2):123–129, 2017.

[96] Rahul Soni and Manivannan Muniyandi. Breath rate variability: a novel measure to study the meditation effects. *International journal of yoga*, 12(1):45, 2019.

[97] Pathipati Srihari, G s Vandana, and B s Raghavendra. Measurement and evaluation of human vital sign using 77ghz awr1642 fmcw radar sensor. In *2021 IEEE 18th India Council International Conference (INDICON)*, pages 1–5. IEEE, 2021.

[98] Li Sun, Shuaiming Huang, Yusheng Li, Chen Gu, Hao Pan, Hong Hong, and Xiaohua Zhu. Remote measurement of human vital signs based on joint-range adaptive eemd. *IEEE Access*, 8:68514–68524, 2020.

[99] Lionel Tarassenko, Mauricio Villarroel, Alessandro Guazzi, João Jorge, David A. Clifton, and Christopher Pugh. Monitoring of vital signs for assessing respiratory function. *Biomedical Engineering Online*, 13(1):82, 2014.

[100] A. Tekleab and M. Sanduleanu. Vital signs detection using fmcw radar. In *2022 International Conference on Electrical and Computing Technologies and Applications (ICECTA)*, pages 51–54. IEEE, 2022.

[101] Axel Trange. Fmcw mmwave radar for detection of pulse, breathing and fall within home care, 2021.

[102] Anton M Unakafov, Sebastian Möller, Igor Kagan, Alexander Gail, Stefan Treue, and Fred Wolf. Using imaging photoplethysmography for heart rate estimation in non-human primates. *PLoS One*, 13(8):e0202581, 2018.

[103] Eberhard Von Borell, Jan Langbein, Gérard Després, Sven Hansen, Christine Leterrier, Jeremy Marchant-Forde, Ruth Marchant-Forde, Michela Minero, Elmar Mohr, Armelle Prunier, et al. Heart rate variability as a measure of autonomic regulation of cardiac activity for assessing stress and welfare in farm animals—a review. *Physiology & behavior*, 92(3):293–316, 2007.

[104] Brahim Walid and Jianhua Ma. Accuracy assessment and improvement of fmcw radar-based vital signs monitoring under practical scenarios. In *2022 IEEE Intl Conf on Dependable, Autonomic and Secure Computing, Intl Conf on Pervasive Intelligence and Computing, Intl Conf on Cloud and Big Data Computing, Intl Conf on Cyber Science and Technology Congress (DASC/PiCom/CBDCom/CyberSciTech)*, pages 1–6. IEEE, 2022.

[105] M.B. Wallén, D. Hasson, T. Theorell, B. Canlon, and W. Osika. Comparison of the polar h10 and the ecg holter for hrv assessment at rest. *European Journal of Applied Physiology*, 119(9):2085–2094, 2019.

[106] Fu-Kang Wang, Ji-Xun Zhong, and Ju-Yin Shih. Iq signal demodulation for non-contact vital sign monitoring using a cw doppler radar: A review. *IEEE Journal of Electromagnetics, RF and Microwaves in Medicine and Biology*, 6(4):449–460, 2022. doi:10.1109/JERM.2022.3214753.

[107] Jingyu Wang, Xiang Wang, Lei Chen, Jiangtao Huangfu, Changzhi Li, and Lixin Ran. Noncontact distance and amplitude-independent vibration measurement based on an extended dacm algorithm. *IEEE Transactions on Instrumentation and Measurement*, 63(1):145–153, 2013.

[108] Pengfei Wang, Yangyang Ma, Fulai Liang, Yang Zhang, Xiao Yu, Zhao Li, Qiang An, Hao Lv, and Jianqi Wang. Non-contact vital signs monitoring of dog and cat using a uwb radar. *Animals*, 10(2):205, 2020.

[109] Pengfei Wang, Yang Zhang, Yangyang Ma, Fulai Liang, Qiang An, Huijun Xue, Xiao Yu, Hao Lv, and Jianqi Wang. Method for distinguishing humans and animals in vital signs monitoring using ir-uwb radar. *International Journal of Environmental Research and Public Health*, 16(22):4462, 2019.

[110] Siying Wang, Antje Pohl, Timo Jaeschke, Michael Czaplik, Marcus Köny, Steffen Leonhardt, and Nils Pohl. A novel ultra-wideband 80 ghz fmcw radar system for contactless monitoring of vital signs. In *2015 37th Annual International Conference of the IEEE Engineering in Medicine and Biology Society (EMBC)*, pages 4978–4981. IEEE, 2015.

[111] Yong Wang, Wen Wang, Mu Zhou, Aihu Ren, and Zengshan Tian. s. *Sensors*, 20(10):2999, 2020.

[112] Mingxu Xiang, Wu Ren, Weiming Li, Zhenghui Xue, and Xinyue Jiang. High-precision vital signs monitoring method using a fmcw millimeter-wave sensor. *Sensors*, 22(19):7543, 2022.

[113] Qingsong Xie, Guoxing Wang, and Yong Lian. Heart rate estimation from ballistocardiography based on hilbert transform and phase vocoder. In *2018 IEEE Asia Pacific Conference on Circuits and Systems (APCCAS)*, pages 139–142. IEEE, 2018.

[114] Hanchun Yang, Yunlong Luo, Alex Qi, Miao Miao, and Yihong Qi. Fmcw-radar-based vital-sign monitoring of pet. In *2021 13th International Symposium on Antennas, Propagation and EM Theory (ISAPE)*, pages 1–3. IEEE, 2021.

[115] Zhenhao Yang and Zengdi Bao. Short-time heart rate estimation based on 60-ghz fmcw radar. In *2023 IEEE MTT-S International Wireless Symposium (IWS)*, pages 1–3. IEEE, 2023.

[116] S. Yoo, S. Ahmed, S. Kang, D. Hwang, J. Lee, J. Son, and S. H. Cho. Radar recorded child vital sign public dataset and deep learning-based age group classification framework for vehicular application. *Sensors*, 21(7):2412, 2021.

[117] Renyuan Zhang and Siyang Cao. Real-time human motion behavior detection via cnn using mmwave radar. *IEEE Sensors Letters*, 3(2):1–4, 2018.

[118] Yuan Zhao, Yunxue Liu, and Zhuoran Cai. A novel scheme for vital sign detection with fmcw radar. In *2022 Global Reliability and Prognostics and Health Management (PHM-Yantai)*, pages 1–6. IEEE, 2022.

[119] Fang Zhu, Kuangda Wang, and Ke Wu. A fundamental-and-harmonic dual-frequency doppler radar system for vital signs detection enabling radar movement self-cancellation. *IEEE Transactions on Microwave Theory and Techniques*, 66(11):5106–5118, 2018.

# Appendix A

# Dataset Article

The following information is created for publishing the dataset of the 10 participants in a journal, which has not been published yet by the time of this report. The title of the article is *Comprehensive mm-Wave FMCW Radar Dataset for Vital Sign Monitoring: Embracing Extreme Physiological Scenarios*, and the authors are Ehsan Sadeghi, Karina Skurule, Alessandro Chiumento, and Paul Havinga.

## A.1 Introduction

Monitoring vital signs, including heart rate (HR) and respiratory rate (RR), plays a pivotal role in the management and prevention of numerous health conditions. Traditionally, such monitoring has been carried out within hospital settings, with established protocols reflecting the importance of these parameters in assessing patient health [59]. However, in some cases patient vital sign monitoring at home is required [66]. Wearable monitoring systems are widely used because of their low costs and accuracy. There has been a significant increase in the development and use of wearable devices for monitoring vital signs in humans. Wearable devices such as smartwatches (like the VitalTracer and the Fitbit) and chest straps can continuously monitor vital signs and provide real-time feedback to the user. Non-wearable devices such as camera-based systems [10, 65], radar systems [54], and hybrid systems [32, 78] have also been developed to monitor vital signs in humans in a non-invasive way.

Radar technology has emerged as a promising technology for vital sign monitoring. The benefits include the elimination of the need for direct skin contact and disrobing, along with radars' reduced sensitivity to environmental factors such as light, temperature, and humidity, in contrast to other non-wearable sensors like cameras and infrared sensors. Furthermore, radar-based sensing addresses existing privacy concerns and issues present with other non-invasive technologies, such as cameras [83]. In literature, the utilization of radar technology for vital sign detection has demonstrated promising outcomes and holds the potential to enhance the management of various medical conditions. To this end, researchers have employed different types of radar systems to investigate challenges associated with vital sign detection. For instance, ultra wide band radar operating at 24GHz [84], stepped frequency continuous wave radar spanning 2-4GHz [79], continuous wave radar at 14GHz [53], and millimeter Wave (mm-wave) Frequency Modulated Continuous Wave (FMCW) radar operating between 75-85GHz [110] have been explored.

8.09%, and BR Error rate is 6.89%. Within the spectrum of radar technologies, FMCW radar has gained significant attention for its proficiency in determining the distance, angle, and speed of objects. Specifically, mm-wave FMCW radar, operating within the higher

frequency ranges of 30 GHz to 300 GHz (corresponding to wavelengths of 1 mm to 10 mm), significantly enhances radar resolution. Additionally, mm-wave FMCW radar offers enhanced privacy in indoor settings, thanks to its high signal attenuation. This technology utilizes subtle chest movements caused by HR and RR to accurately estimate vital signs. The exceptional sensitivity of mm-wave FMCW radar facilitates precise measurements of chest displacement, thereby yielding more accurate estimations of HR and RR.

There are existing datasets of vitals sign recordings by a radar and a reference sensor. Schellenberger, S., et al. [86], have recorded 24-hour data from 30 healthy subjects by using a 24 GHz continuous wave radar and Electrocardiography (ECG), blood pressure sensor, and Impedance Cardiogram (ICG) as a reference. Five scenarios were carried out, where the aim was to trigger the autonomic nervous system and hemodynamics of the subject. Yoo, Sungwon, et al. [116] have published an FMCW radar recorded dataset of vitals signs for 50 children. Tekleab, Aaron, and Mihai Sanduleanu [100] have published a dataset for which a mm-wave FMCW radar was used. The test subjects were 4 children under the age of 13. To the best of our knowledge, no publicly available dataset utilizes mm-wave FMCW radar for the detection of vital signs in adults.

This paper presents the first comprehensive dataset leveraging mm-wave FMCW radar for the non-invasive monitoring of HR and respiratory rate RR in adults. Our investigation assesses the radar's accuracy by comparing its measurements against those obtained from the Polar H10, a reference sensor renowned for its precision. Various scenarios, including distance, angle, orientation, and elevated heart rate situations, were considered. Data from ten participants was collected, where four of the participants took part in an elevated heart rate scenario. The experiment aimed to investigate the capabilities of FMCW radar in diverse real-world situations, providing insights into its potential applications. The contributions of this dataset are as follows:

- **Diverse Participant Pool:** The dataset encompasses recordings from 10 adults, highlighting a variety of demographic groups and physical conditions. This includes:
  - Individuals with asthma and an experienced meditator, showcasing the radar's capability to capture data across extreme physiological conditions.
  - Participants with elevated heart rates due to cardio exercise, further diversifying the dataset's applicability.

- **Diverse Evaluation Scenarios**:
  - Emulate real-world applications: Through a series of meticulously designed scenarios—including variations in distance, angle, orientation, and conditions of elevated HR—we aim to emulate real-world applications.
  - Carefully designed scenarios enable a comprehensive evaluation of radar performance across varying distances, angles, and orientations, reflecting real-world conditions. This approach takes into consideration the specific radar characteristics, features, and antenna patterns, ensuring a thorough assessment of its capabilities in practical applications.

- **Inclusion of Extreme Cases:** Our study uniquely incorporates data from participants with extreme physiological conditions—post-exercise (elevated HR and RR), asthma (high RR), and experienced meditators (low RR)—to demonstrate the radar's effectiveness in real-world scenarios. This approach highlights its capability to accurately detect vital signs across a broad range of conditions.

- **Preliminary Validation Through Case Study:** To demonstrate the practical utility and precision of our dataset, we provide initial findings from a detailed case study of one participant. This example highlights the mm-wave FMCW radar's efficacy in accurately monitoring cardiovascular and respiratory systems. These early results serve not only to validate the integrity of the data collected but also to emphasize the radar's potential for non-invasive, precise vital sign monitoring.

In the subsequent sections of this paper, we delve into the methodology, participant profiles, scenarios, data formatting, and initial validation efforts in detail. This structure aims to equip other researchers with the necessary information to effectively utilize our dataset, ensuring its reusability and facilitating rigorous testing of its validity for their own studies.

## A.2  Methodology

### A.2.1  Instrumentation and Setting

In this experiment, we utilized millimeter-wave (mm-wave) Frequency-Modulated Continuous Wave (FMCW) radar. The Texas Instruments (TI) AWR1642BOOST radar automotive radar sensor evaluation module (EVM) was employed for this purpose [42]. To facilitate the collection of raw data, it was necessary to use the complementary DCA1000 board to capture ADC raw samples of the radar's intermediate frequency (IF) signal[43]. Both AWR1642 EVM and DCA 1000 used in this experiment can be seen in Fig A.1. Moreover, we designed a radar holder to ease the data collection procedure. This configuration leverages the full potential of the radar system. For instance, by utilizing the entire bandwidth, we aimed to achieve the highest possible range resolution. This principle is mathematically formulated as $d_{\text{res}} = \frac{C}{2BW}$, where $C$ denotes the speed of light $(3 \times 10^8$ m/s), $d_{\text{res}}$ represents the range resolution, and $BW$ is the bandwidth utilized by the radar. In our experiment, the full bandwidth of 4 GHz was employed, enhancing the radar's capability to distinguish between closely spaced objects in distance.

It is important to note that the AWR1642 is utilized in a Multiple Input Multiple Output (MIMO) mode. This configuration enables us to harness various MIMO benefits, such as enhanced spectral efficiency and improved signal quality due to diversity gain. These advantages are critical for achieving high-resolution and reliable radar sensing capabilities.

Additionally, as a reference sensor for heart rate measurements, the Polar H10 heart rate sensor was employed. The Polar H10 is considered a trustworthy reference sensor for heart rate measurement due to its superior accuracy compared to other devices and Holter monitors tested, as evidenced by extensive validation tests. These tests demonstrated that the H10, when used with the Pro Strap, offered the best heart rate measurement accuracy among all tested systems. Specifically, it detected RR intervals with a precision of within 2 milliseconds accuracy for 92.9% in running, 99.3% in cycling, 95.3% in weight training, and 95.6% across all activities combined, showcasing its exceptional performance and reliability across various exercise conditions [73].

In the data acquisition section, which we elaborate on later, we detail our method for collecting reference values for the respiratory rate. To achieve this, we divided our observation period into one-minute intervals. Participants were instructed to meticulously count their breaths, including both inhalations and exhalations, to ensure precision. Additionally, to validate the values reported by participants, we employed a high-resolution camera specifically focused on the abdominal and chest areas. This approach allowed for a more accurate verification of the respiratory rates provided by the subjects.

TABLE A.1: Configuration Parameters of AWR1642BOOST

| Parameter | Value |
|---|---|
| Start Frequency | 77 GHz |
| End Frequency | 81 GHz |
| ADC Start time | 6 $\mu$s |
| ADC Samples | 250 |
| Sample Rate | 6250 ksps |
| Ramp End Time | 50 $\mu$s |
| Idle Time | 7 $\mu$s |
| Chirp Count | 1 |
| Frame Count | 1200 |
| Frame Periodicity | 50 ms |
| Chirp Loop Count | 128 |
| RX Gain | 30 dB |
| TX Count | 2 |
| RX Count | 4 |



FIGURE A.1: From right to left: AWR1642 EVM- DCA1000- AWR1642 and DCA1000 in the designed radar holder.

FIGURE A.2: 3D View of the room ZI-5038 and the experimental setup.

## A.2.2 Research Experiment Location

The experiments took place in Room ZI-5038, located within the Pervasive Systems group at the Edge Center on the fifth floor of the Zilverling building, part of the Faculty of Electrical Engineering, Mathematics, and Computer Science (EEMCS) at Twente University, Enschede, the Netherlands. A detailed 3D layout of the room, including the location of the devices used and the positioning of participants, is illustrated in Fig. A.2. Participants were seated on chairs set approximately 45 centimeters above the floor, while the radar was strategically positioned so that its antennas were about 90 centimeters from the ground. To facilitate participant involvement in each scenario, the room and setup were prearranged and labeled, as will be further detailed later in the text.

Minor but important to note, our measurements were conducted during the winter season, a detail of particular importance due to its influence on the clothing thickness of participants. Winter attire, generally bulkier and composed of denser materials, can significantly impact radar signal attenuation and reflection. Such clothing increases signal attenuation, as the materials may absorb or reflect a greater portion of the radar signal, potentially affecting the accuracy of vital sign detection. The dielectric properties of heavier winter clothing could also alter the radar signal's interaction, modifying signal penetration and the characteristics of the reflected signal, including crucial Doppler shifts used for assessing heart rate and respiration. Given these considerations, the outcomes observed in our study, despite the potential for increased signal attenuation due to winter clothing, suggest that the radar-based system possesses robust detection capabilities. Moreover, this implies that experiments conducted with less clothing—resulting in reduced attenuation—might yield even more pronounced results, further demonstrating the efficacy of the mm-wave FMCW radar in diverse conditions.
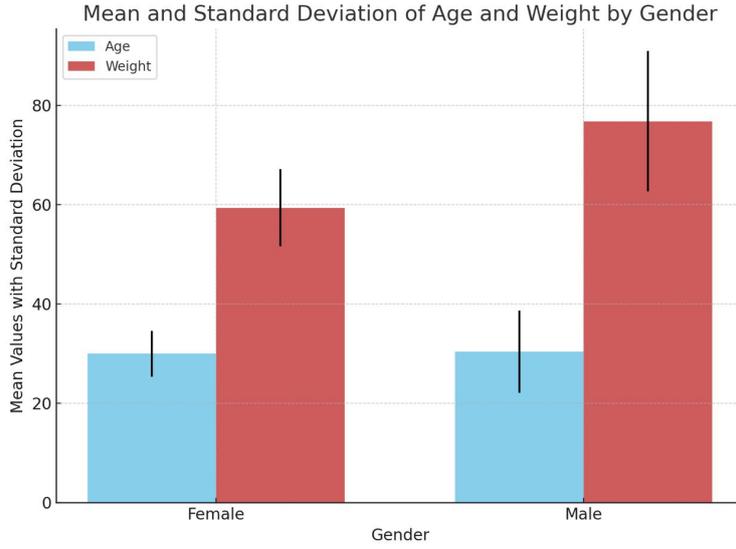
FIGURE A.3: Mean and Standard deviation for age and weight among participants.

## A.3 Participant Information

### A.3.1 Participant Demographics

A total of 10 participants were recruited for the measurement sessions, comprising an equal distribution of 5 males and 5 females. Prior to their involvement, all participants were fully briefed on the procedures and objectives of the study and provided informed consent by signing a consent form.

The participants' weights and ages were recorded, with the mean weight and age being:

$$\bar{x}_{\text{weight}} = 68.1 \text{ kg} \tag{A.1}$$
$$\sigma_{\text{weight}} = 14.14 \text{ kg} \tag{A.2}$$
$$\bar{x}_{\text{age}} = 30.2 \text{ years} \tag{A.3}$$
$$\sigma_{\text{age}} = 6.32 \text{ years} \tag{A.4}$$

The distribution of both age and weight is summarized in Fig. A.3 for a comprehensive overview. Each of the 10 participants took part in the distance, orientation, and angle scenarios to assess the radar's performance under varying conditions. Furthermore, a subset of four participants also engaged in the elevated HR scenario, details of which are tabulated in Table A.2. This diverse participant pool ensures a broad representation of data for analyzing the radar's effectiveness across different demographic groups and physical conditions.

TABLE A.2: List of participants as well as their gender, age, and engagement in different scenarios.

| Participant number | Gender | Age | Weight | Engaged Scenarios |
|---|---|---|---|---|
| Participant 1 | Male | 22 | 83 | Distance, Orientation, Angle |
| Participant 2[1] | Male | 27 | 70 | Distance, Orientation, Angle, Elevated |
| Participant 3 | Female | 30 | 60 | Distance, Orientation, Angle, Elevated |
| Participant 4 | Female | 25 | 63 | Distance, Orientation, Angle, Elevated |
| Participant 5[2] | Female | 26 | 54 | Distance, Orientation, Angle |
| Participant 6[2] | Male | 31 | 98.5 | Distance, Orientation, Angle, Elevated |
| Participant 7 | Female | 33 | 70 | Distance, Orientation, Angle |
| Participant 8 | Male | 28 | 63 | Distance, Orientation, Angle |
| Participant 9 | Female | 36 | 50 | Distance, Orientation, Angle |
| Participant 10 | Male | 44 | 69.5 | Distance, Orientation, Angle |

[1] Participant with extensive experience in meditation.

[2] Participant diagnosed with asthma.

### A.3.2 Special Participant Profiles

In our study, special consideration was given to examining the radar's performance across a range of physiological extremes, including both unusually low and high respiratory rates. To this end, our participant selection included individuals at opposite ends of the respiratory rate spectrum: those with asthma, characterized by higher than average RR, and a participant experienced in meditation, known for significantly lower RR.

This approach allowed us to include two distinct cases within our dataset: firstly, two participants suffering from asthma, which often results in an elevated respiratory rate, especially during acute attacks. Such conditions are expected to test the radar's sensitivity to faster breathing patterns. Research has consistently shown that asthmatic individuals tend to have a higher baseline RR compared to non-asthmatic counterparts [49].

Secondly, participant number 2, with extensive experience in meditation, presents an intriguing case of abnormally low respiratory rates, with recordings as low as 3.5 breaths per minute (BPM) observed. Meditation is known to profoundly impact respiratory function, primarily reducing the breathing rate. This reduction is attributed to deep relaxation and activation of the parasympathetic nervous system induced by meditation practices. Sony et al. (2019) have explored Breath Rate Variability (BRV) as a novel metric to examine the effects of meditation, suggesting it as a distinguishing factor between meditators and non-meditators [96].

By incorporating these special cases, our goal was to simulate a wide array of real-world situations, ensuring that the developed device can accurately detect vital signs across a diverse population. Through this methodology, we aimed to validate the radar's utility in real-life applications, affirming its capability to adapt to the varying needs of all users.

## A.4 Data Collection Scenarios

The primary objective of these measurements is to explore the capabilities of FMCW radar in non-contact health monitoring, with the ultimate goal of developing a standalone product capable of autonomous health monitoring. In practical applications, FMCW radar has the potential for a wide array of uses, including vital sign detection and activity

recognition. To fully realize this potential, it's crucial to simulate realistic conditions that the radar might encounter in real-world scenarios. This includes situations where the radar is not ideally positioned relative to the subject, such as not facing the chest area directly.

To address this, we have devised a series of distinct scenarios to rigorously test the radar's accuracy and reliability under various conditions. These scenarios involve varying the distance, angle, and orientation of human participants relative to the radar. Additionally, our study extends to assessing the radar's performance under specialized conditions. This includes gathering data from individuals with asthma to understand the radar's sensitivity to varying respiratory patterns. We also focus on scenarios involving elevated heart and breathing rates, achieved by having participants engage in physical activities like climbing stairs. These scenarios are vital for evaluating the radar's effectiveness in dynamic, real-world conditions where physiological parameters may deviate from the norm due to various activities or health conditions.

Such a comprehensive evaluation aims to deepen our understanding of the radar's performance across different settings and identify strategies to maintain or enhance accuracy in less-than-ideal conditions. Below, we detail the purpose and methodology of each scenario, providing insights into our experimental approach and the rationale behind it.

### A.4.1 Distance Scenario

The mmWave FMCW radar operates in a frequency range that uniquely balances advantages against challenges. A significant advantage of mmWave frequencies is the enhancement of privacy, given that signals typically do not penetrate walls, thus minimizing the risk of data interception. Nonetheless, this characteristic contributes to higher signal attenuation as the distance from the radar source increases, presenting a unique set of challenges [77].

As distance grows, the power of the desired signal tends to wane, and concurrently, the noise level within the signal may ascend. This dynamic shift leads to a reduced Signal-to-Noise Ratio (SNR), complicating the task for signal processing algorithms to accurately estimate vital signs such as HR and RR. Recognizing the critical nature of these challenges, this scenario is dedicated to scrutinizing the radar's efficacy and the precision of HR and RR estimations across varying distances. Grasping the extent to which signal attenuation influences data quality is paramount for the development of robust health monitoring applications leveraging FMCW radar technology.

In this experimental setup, participants were seated at specific distances from the radar — 40 cm, 80 cm, 120 cm, and 160 cm — with their chest area oriented directly towards the radar apparatus. To ensure the purity of data collection, participants were advised to remain motionless, thereby reducing the potential for data interference.

Data was meticulously recorded in four separate one-minute segments for each participant at every prescribed distance. This methodical approach facilitated a comprehensive assessment of how distance impacts both the quality of the signal and the accuracy of the vital sign estimations derived from it. This endeavor aims not only to illuminate the challenges posed by increasing distances but also to identify potential strategies to mitigate these effects, ensuring the radar's applicability in a wide array of health monitoring contexts

### A.4.2 Orientation Scenario

In practical applications, individuals may assume various orientations relative to the radar. Understanding the radar's capabilities and limitations across all possible orientations is

crucial, particularly for deployment in healthcare settings, vehicles, or smart home systems where users might not directly face the radar. To address this, we investigate the impact of orientation on radar performance while maintaining a consistent distance.

Participants are seated at a fixed distance of 80 cm from the radar, facing in different directions rather than directly towards it. This setup allows us to systematically collect data as the front, back, left side, and right side of the participant's body are oriented towards the radar. For each orientation, we record four separate one-minute data sessions.

The orientation of the participant relative to the radar is significant for several reasons. The Radar Cross Section (RCS) varies significantly with body orientation. Typically, the front of the body presents a larger RCS due to the greater surface area facing the radar, resulting in stronger reflected signals. Conversely, the sides and back exhibit a smaller RCS, potentially leading to weaker or differently characterized reflections.

Different orientations also affect signal penetration, reflection, and absorption, altering the characteristics of the received signal. The Line of Sight (LOS) signal carries different information depending on the orientation, and multipath propagation dynamics change accordingly. Orientations other than directly facing the radar are expected to significantly reduce the SNR of the chest displacement pattern, impacting the accuracy of vital sign detection. Additionally, different orientations influence the object's position relative to the main lobe of the antenna pattern and affect Doppler shifts due to chest movements. By understanding these dynamics, we can optimize radar performance and develop algorithms that are robust across various orientations, enhancing the radar's applicability in diverse settings.
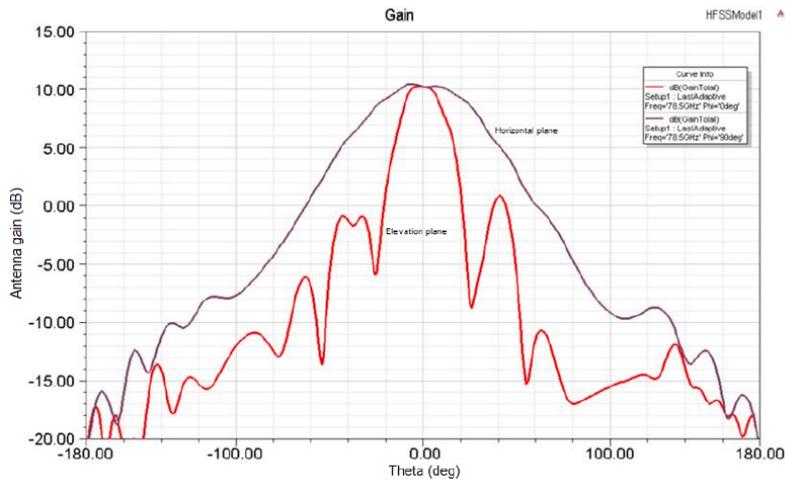
### A.4.3 Angle Scenario



FIGURE A.4: Antenna pattern of AWR1642 EVM [42].

In real-world applications, it's unlikely that subjects will always be perfectly aligned with the radar's direct line of sight. To mimic these realistic conditions and assess the radar's adaptability, testing at various angles is essential.

The antenna pattern of the AWR1642 Evaluation Module (EVM), as depicted in Fig. A.4, illustrates how antenna gain varies with the angle (theta) [42]. This pattern indicates that antenna gain is maximized at 0 degrees and diminishes as the angle widens. Consequently, the most precise vital sign estimations are anticipated at 0 degrees. As the angle

deviates to 30 and 45 degrees, a reduction in signal strength is expected, following the antenna gain pattern. This reduction could lead to a lower SNR of the received signal, potentially impacting the accuracy of HR and RR estimations.

To investigate these effects, data were collected from participants seated at a consistent distance of 80 cm from the desk, on which radar was placed. Participants were positioned with 0, 30, and 45 degrees of deviation on the horizontal plane relative to the radar's normal axis. For each angular setting, four separate one-minute measurements were captured using the radar. It's important to note that participants were oriented towards the desk, not directly facing the radar. This setup more closely simulates real-life scenarios where individuals may not always be ideally positioned towards the radar. Such an approach not only aids in evaluating the radar's performance under varied angular conditions but also contributes to understanding how radar signals reflect off different surfaces and body orientations. Enhancing our understanding of these dynamics is crucial for improving the robustness of algorithms designed for vital sign detection in less-than-ideal conditions.

### A.4.4  Elevated HR Scenario

The elevated HR and RR scenario is designed to assess the radar's capability under conditions of increased physiological activity, such as physical exertion or stress. This evaluation is crucial for ensuring the radar's applicability in real-world scenarios beyond calm, resting states. It particularly focuses on the radar's sensitivity and accuracy in tracking rapid changes in heart rate and respiration rate, which are vital for applications requiring immediate health monitoring or stress detection.

In this scenario, four participants, including one individual with asthma, were selected to induce elevated heart and respiration rates through physical activity. They were instructed to ascend the stairs to the fifth floor of the Zilverling building within the EEMCS faculty at Twente University. Immediately after reaching the designated floor, participants positioned themselves 80 cm in front of the radar, ensuring they were facing towards it, to commence data collection. Two separate one-minute data segments were recorded in this state to capture the elevated physiological rates.

To further assess the radar's performance as heart and respiration rates began to stabilize, participants were not given a rest period. Instead, after the initial two minutes of recording—during which their heart and respiration rates naturally started to return towards normal levels—they were immediately asked to undertake the stair-climbing activity once more. This repetition aimed to induce a second increase in heart and respiration rates, after which another two separate one-minute data recordings were captured using the radar. This iterative approach allows for a nuanced understanding of the radar system's adaptability to rapid physiological fluctuations, offering insights into its potential reliability and effectiveness in dynamic, real-life applications.
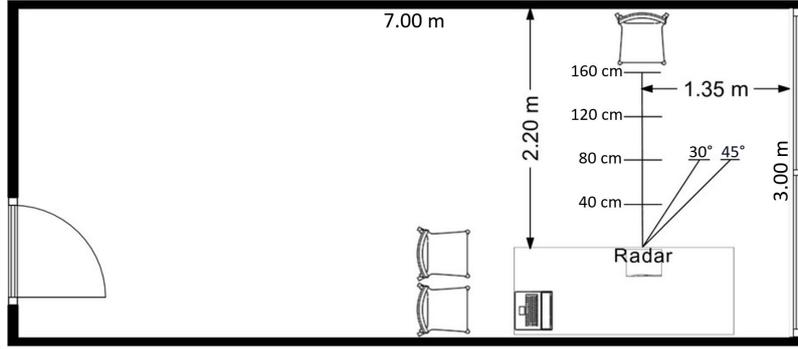
FIGURE A.5: The floor map: dimensions and the experimental setup.

## A.5  Experimental Setup

The radar system, comprising the AWR1642 EVM, DCA1000, and radar holder, was positioned on an office table. Elevation adjustments were implemented to align the radar antenna array with the chest of the seated individual, ensuring consistency across participants. The radar system's location remained constant throughout the study. The participants were sitting on a chair, approximately 45 centimeters from the ground, and the radar was placed in a way that the antennas were located approximately 90 centimeters from the ground. A laptop computer, placed on the same table, established connections with the radar system according to the guidelines outlined in the tutorial [43]. To facilitate smooth transitions between scenarios, demarcations were made on the floor using duct tape to indicate distances of 40 cm, 80 cm, 120 cm, and 160 cm (distance scenario), along with angles of 30 and 45 degrees at a distance of 80 cm from the radar (angle scenario). The setup remained consistent for the elevated scenario, ensuring uniformity across measurements. For the orientation scenario, the chair was strategically rotated to adjust the participant's position relative to the radar, accommodating the varied angles required for this specific set of experiments. To provide a clear understanding of the spatial arrangement and distances utilized in each experimental scenario, a detailed floor map of the room and the entire setup is included. This visual representation can be found in Fig. A.5, offering an invaluable perspective on the physical context of our measurements. Chair movements to specified distances were guided by the tape, ensuring precise positioning. Upon seating, distance validation included a visual alignment check between the tape indication and the participant's chest. In Fig A.6, a participant can be seen while collecting data for the angle scenario.

FIGURE A.6: Participant Demonstrating the Angle Scenario within the Experimental Setup.

## A.6 Data Acquisition

### A.6.1 Data recording procedure

Adjacent to the participant's right side, three individuals, out of the radar's line of sight, facilitated the experiment. One operated the laptop for radar measurements through the TI mm-wave Studio software. The TI mmWave Studio serves as the software for radar and DCA1000 configuration, as well as data recording. Additional software prerequisites included Matlab Runtime Engine V8.5.1 or higher and Code Composer Studio V7.1 or higher. Instructions on the connections and software utilization can be found in the DCA1000 training tutorial [43]. The second ensured synchronized measurements via the Polar Beat application (for more information check the Polar website). The Polar Beat software application on an Android phone facilitated the recording of all measurements. The heart rate sensor was paired with the Polar Beat app through Bluetooth to ensure accurate and synchronized heart rate data collection. Finally, the third counted breaths and recorded 1-minute high-resolution video recordings of the participant's chest area. Video documentation was initiated in case breath counts required verification. At the end of each 1-minute measurement, the participant reported the breath count, and it was cross-validated with the third person's count. Later verification through recorded high-resolution videos was done to ensure the accuracy of the reported breath count.

### A.6.2 Participant Preparation

Prior to commencing measurements, participants were provided with an informed consent form, which, upon signing, was followed by a concise explanation of the primary objectives of the study. Subsequently, participants were directed to affix the Polar H10 heart rate sensor directly onto their skin, positioned just below the sternum. Verification of a secure connection between the heart rate sensor and the phone running the Polar Beat application was conducted to ensure reliable heart rate measurements. Following the sensor setup, participants were guided to take a seat on a chair positioned in front of the radar,

corresponding to the first measurement scenario. Participants were instructed to minimize body movements during measurements, with no specific guidelines regarding breathing rate—participants were neither directed to maintain a normal nor abnormal rate. However, they were prompted to count their breaths during the 1-minute measurements and articulate the results aloud upon completion for recording purposes. Note that the participants were asked to account for both exhalation and inhalation, ensuring the inclusion of incomplete breaths in our analysis. Post each scenario, participants were asked to stand while the chair was relocated to the next setup for subsequent measurements. This procedural approach maintained consistency across scenarios and facilitated a smooth transition between measurement configurations. It should be noted that all distances mentioned are measured from the chest area to the antenna patch, ensuring precision in the spatial configuration of our experiments.

### A.6.3 Data format

#### FMCW mm-wave Radar

In the data collection process using the FMCW Miniature Radar, the file size is determined by the number of ADC samples, the number of receive channels, the number of frames, the number of chirps, and the number of bytes per sample. Based on the radar configuration, the formula used to calculate the expected file size is as follows:

$$\text{Total Size in Bytes} = N_{ADC} \times N_{RX} \times N_{Frames} \times N_{Chirps} \times B_{Sample} \tag{A.5}$$

where $N_{ADC}$, $N_{RX}$, $N_{Frames}$, $N_{Chirps}$, and $B_{Sample}$ represent the number of ADC samples, receive channels, frames, chirps per frame, and bytes per sample, respectively. This formulation succinctly captures the total approximate memory required to store the captured ADC data. For our specific setup, with 250 ADC samples, 4 receive channels, 1200 frames, 128 chirps, and 4 bytes per sample (accounting for IQ demodulation where each sample consists of 2 bytes for I and 2 bytes for Q), the calculated file size is approximately 614,400,000 bytes, or 585.94 megabytes. The slight discrepancy observed, with the actual file size being around 600 megabytes, is within acceptable limits. This difference can often be attributed to file system overhead, the inclusion of metadata within the file, or the formatting of the data storage. Such a marginal discrepancy is not uncommon and does not generally indicate any issues with the data integrity or the radar's performance. It is important to note that this calculation assumes a seamless data collection process without any additional data or headers that might be included in the file. The order of IQ samples from each receiver and LVDS lanes are explained in detail in Fig A.7. More details can be found in the DCA1000EVM user's guide and TI mmWave radar application report [43, 42].
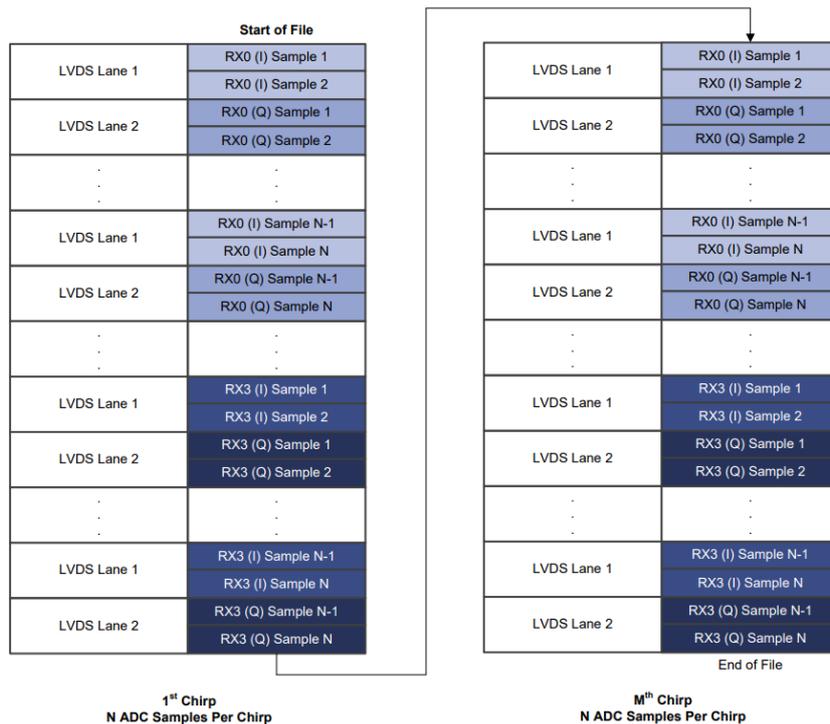
FIGURE A.7: xWR16xx/IWR6843 Complex Data Format Using DCA1000 [43].

## Polar H10

The reference heart rate measurements were obtained using the Polar Beat application, with synchronization facilitated by the Polar Flow application. Saving and accessing the recordings were accomplished through the Polar Flow website. Within the website's diary section, data could be preserved by utilizing the "Export session" option and selecting the export training session as a CSV file. The approximate size of the file is 2 KB. The CSV file structure comprises three initial rows containing recording details. Row 1 delineates parameter names, including name, sport, date, start time, duration, etc. Row 2 corresponds to parameter values aligned with the categories in Row 1. Row 3 specifies parameter names such as sample rate, time, HR (bmp), etc. Subsequent rows consist of parameter values related to the parameters outlined in Row 3, with only two parameters - time and HR in beats per minute (bmp). The format of rows 4 to 63+ is *,00:00:01,73,,,,,,,,,*, where the time (*00:00:01*) of the measurement is in column 2, and the heart rate (*73*) is recorded in column 3. Each recording was made for the time between *00:00:00*, and stopped between time stamps *00:00:59* and *00:01:02*, hence the amount of rows in the recorded CSV files vary between 63 and 66 rows.

Ultimately, following verification with recordings from a high-resolution camera, the breath count reported for each participant was meticulously documented in an Excel sheet.

# Appendix B

# Micro-Doppler Spectrogram Examples
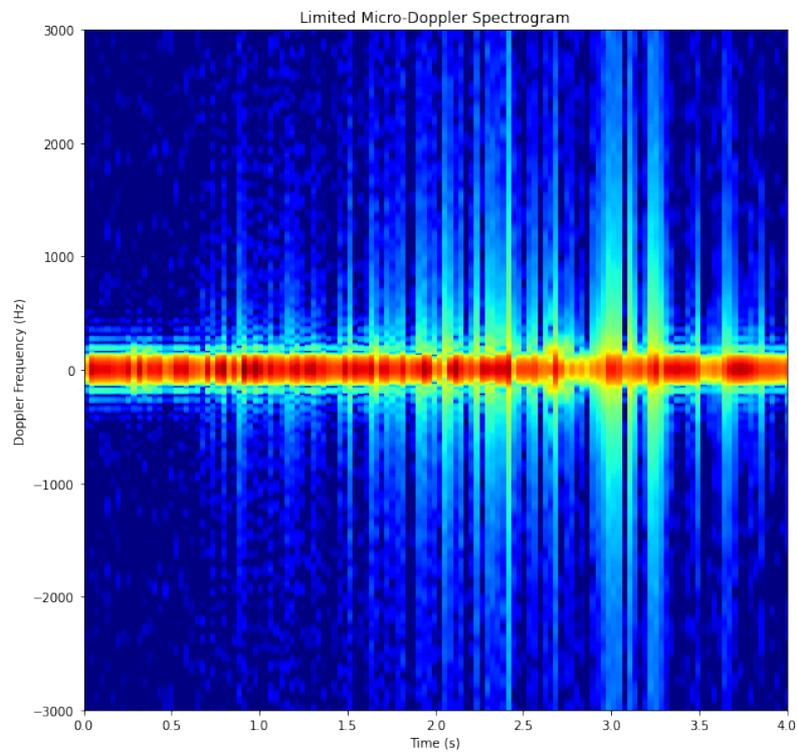


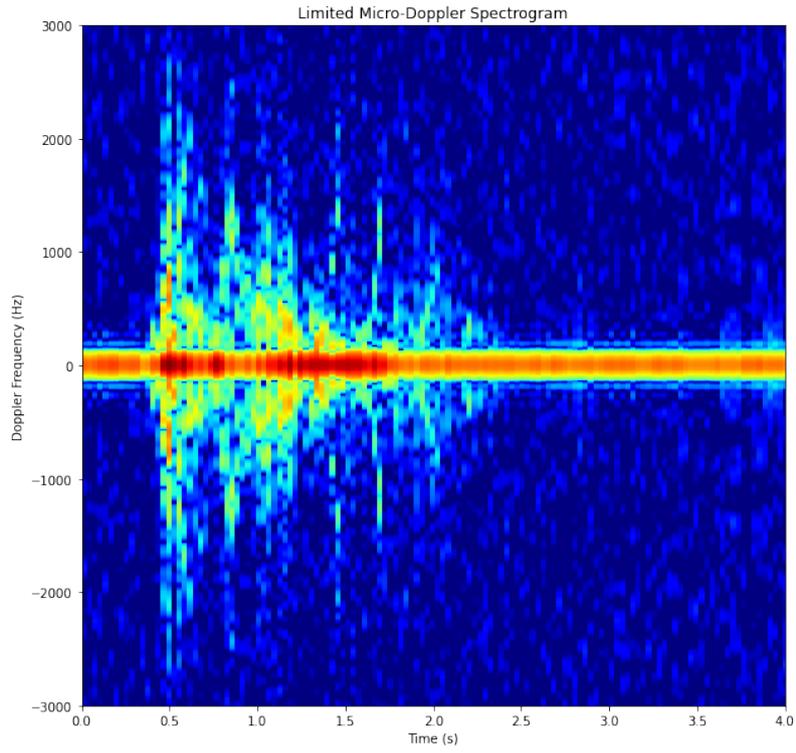FIGURE B.1: Micro-Doppler Spectrogram of Cat Eating.

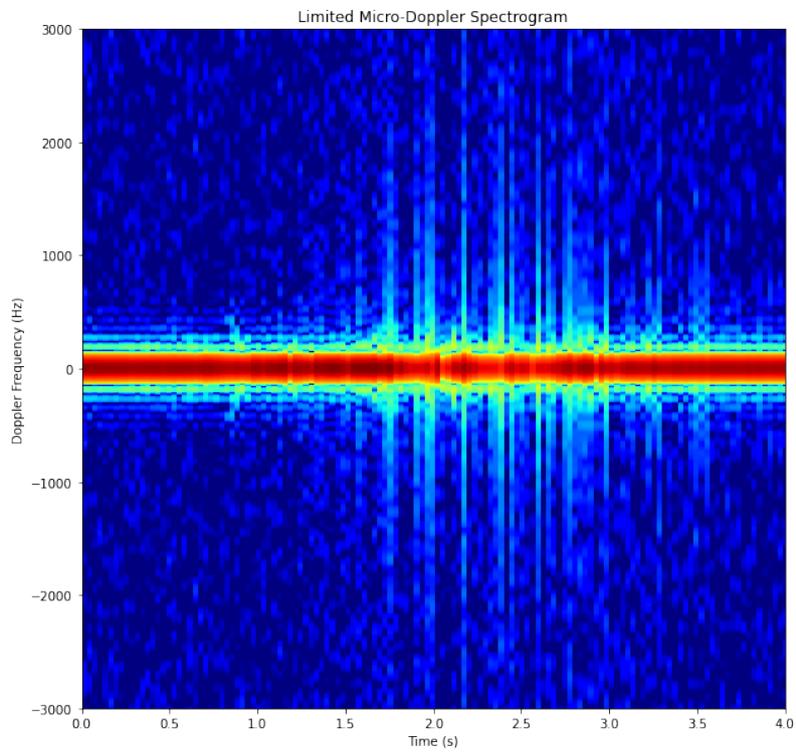FIGURE B.2: Micro-Doppler Spectrogram of Cat Jumping.



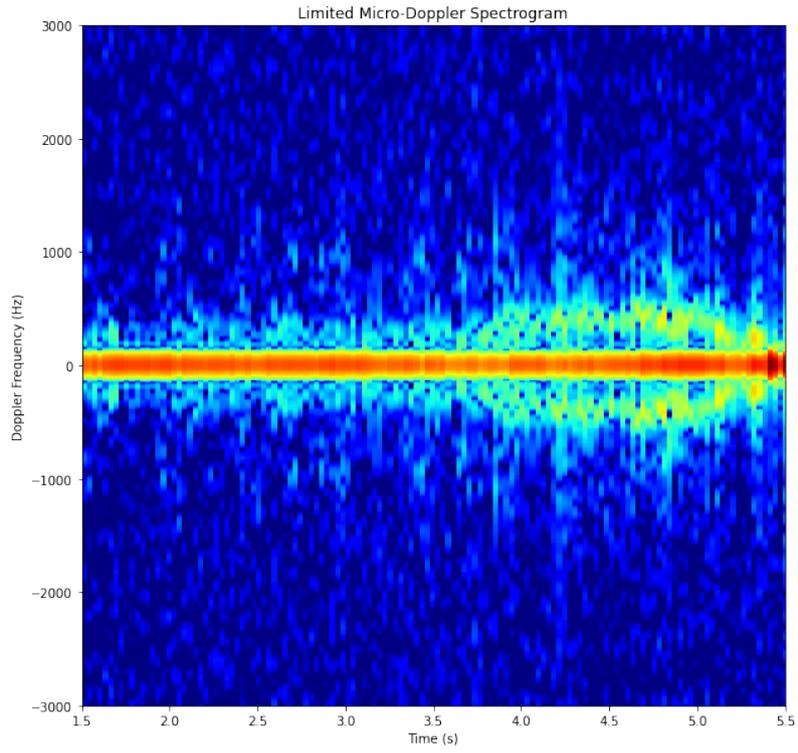FIGURE B.3: Micro-Doppler Spectrogram of Cat Walking By.

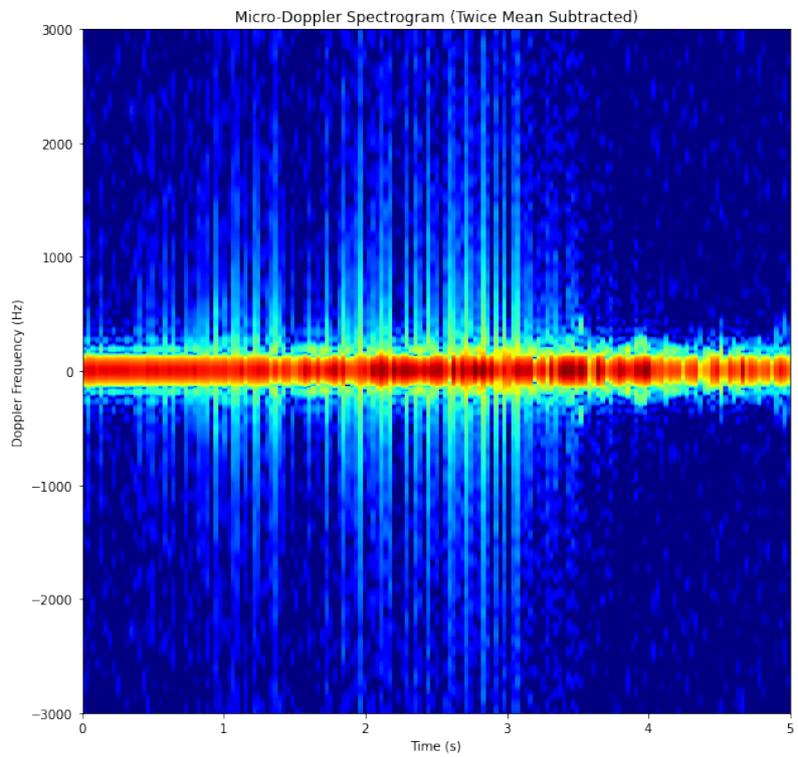FIGURE B.4: Micro-Doppler Spectrogram of Cat Walking Towards.



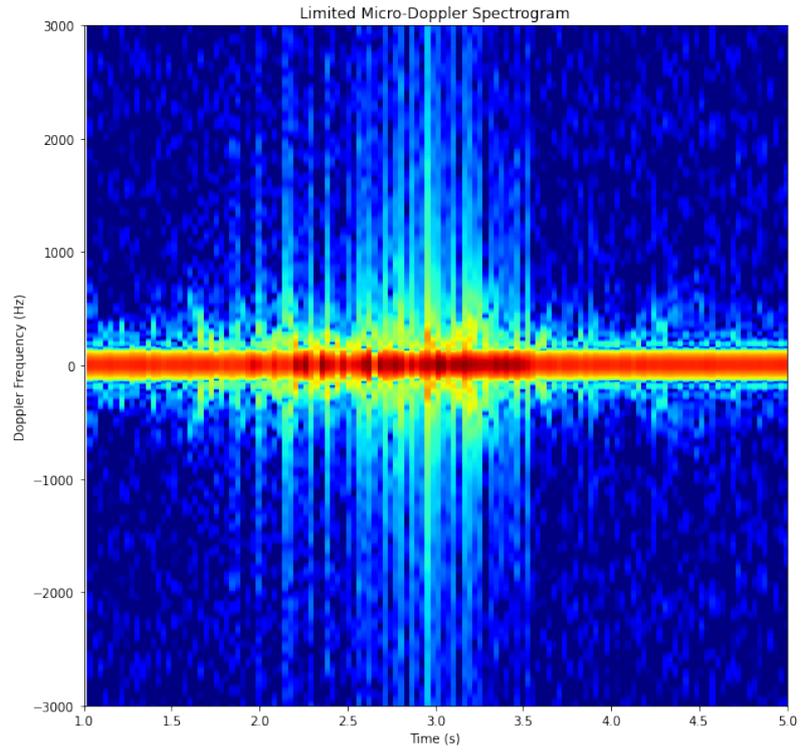FIGURE B.5: Micro-Doppler Spectrogram of Cat Walking with a Human.

FIGURE B.6: Micro-Doppler Spectrogram of a Human Walking.
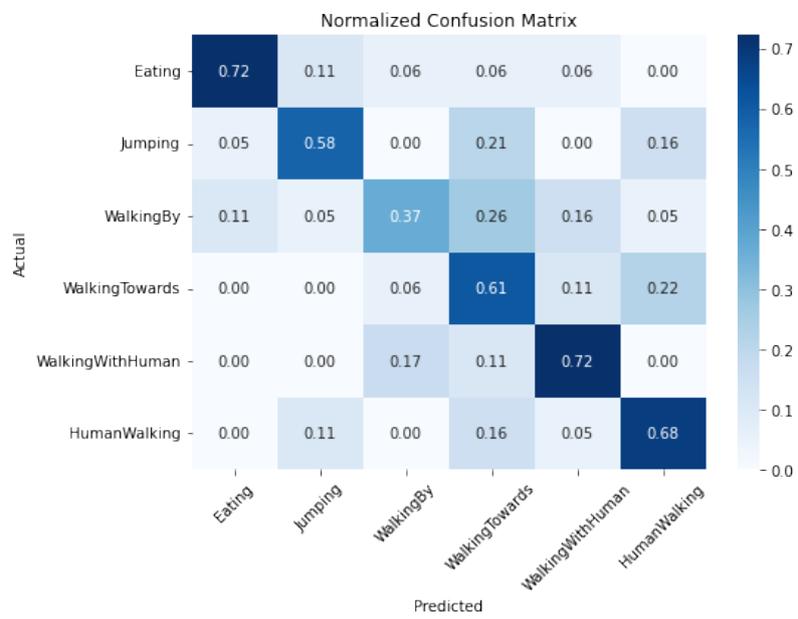
# Appendix C

# Classifier Test Confusion Matrices



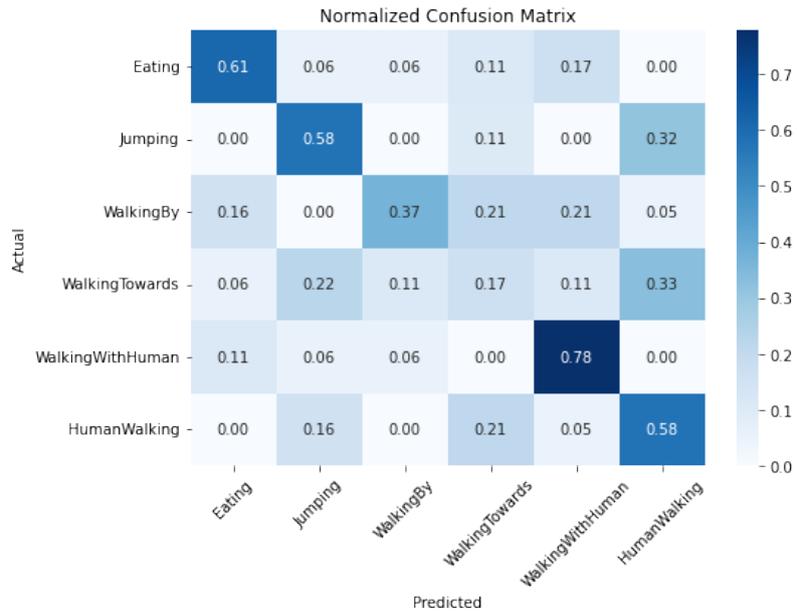FIGURE C.1: CNN + LSTM Test Confusion Matrix.
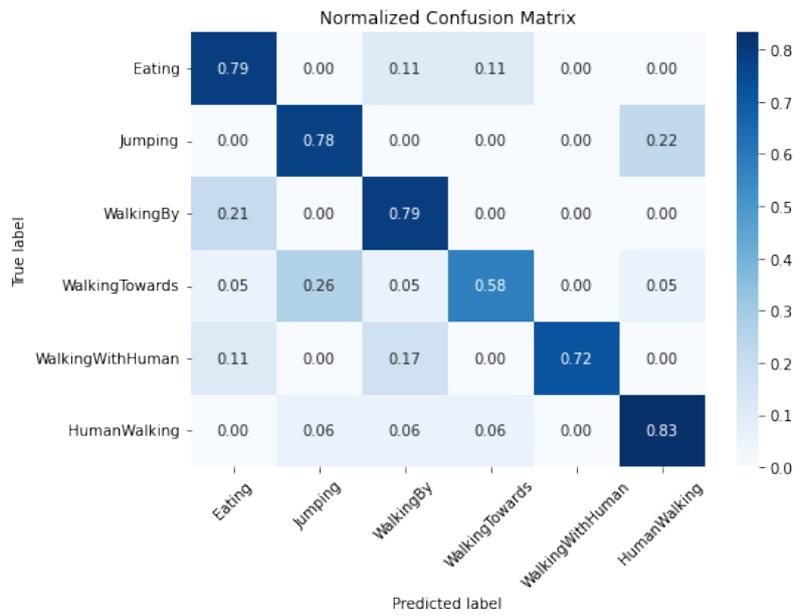
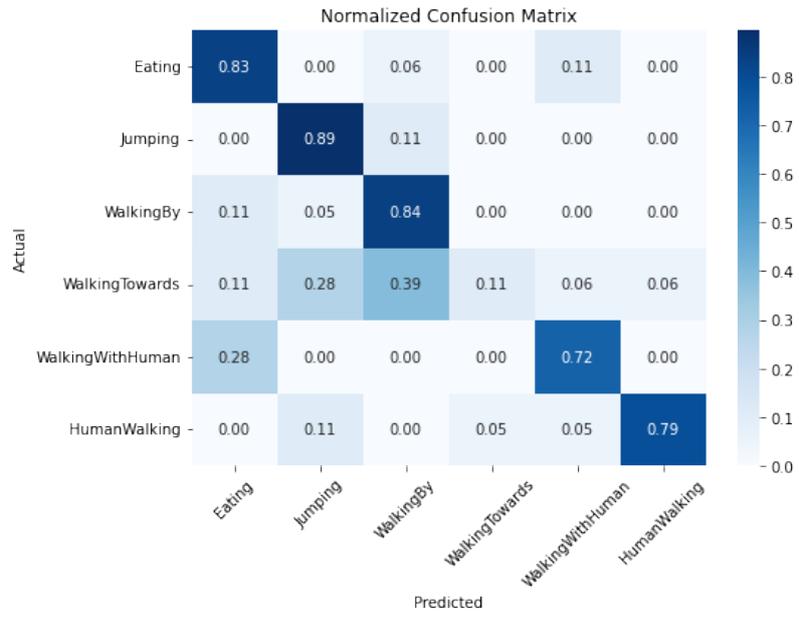FIGURE C.2: LSTM Test Confusion Matrix.



FIGURE C.3: SVM Test Confusion Matrix.

FIGURE C.4: MLP Test Confusion Matrix.